



Large-scale CO ($J=1-0$) Observations toward the M120.1+3.0 Molecular Cloud: A Filament with a Chain of Starburst Clusters

Li Sun^{1,2}, Xuepeng Chen^{1,2}, Jiancheng Feng^{1,2}, Min Fang^{1,2}, Shiyu Zhang^{1,2}, Weihua Guo^{1,2}, Yan Sun^{1,2},
Yang Su^{1,2}, Shaobo Zhang¹, Miaomiao Zhang¹, Xiao-Long Wang¹, Qing-Zeng Yan¹, Xin Zhou¹, and Ji Yang^{1,2}
¹Purple Mountain Observatory, and Key Laboratory of Radio Astronomy, Chinese Academy of Sciences, Nanjing 210023, China; lisun@pmo.ac.cn,
xpchen@pmo.ac.cn

²School of Astronomy and Space Science, University of Science and Technology of China, Hefei 230023, China
Received 2022 September 25; revised 2022 November 8; accepted 2022 November 14; published 2023 January 11

Abstract

We present large-scale ($2^\circ \times 2^\circ$) observations toward the molecular cloud M120.1+3.0, using ^{12}CO , ^{13}CO and C^{18}O ($J=1-0$) data from the Purple Mountain Observatory 13.7 m millimeter telescope. The distance of the cloud is measured to be ~ 1.1 kpc. Using the ^{13}CO data, we identify a main filament F1 and two sub-filaments F2 and F3 in the cloud, which together show a “hub-filament” structure. Filaments F1 and F2 are thermally supercritical. Furthermore, F1 displays clear localized systematic motions in the ^{13}CO position–velocity diagram, which could be explained by accretion along the filament. The mean estimated accretion rate is $\sim 132 M_\odot \text{Myr}^{-1}$. Approximately 150 ^{13}CO clumps are identified in the cloud, of which 39 are gravitationally bound. Most of these virialized clumps are well distributed along the supercritical filaments F1 and F2. Based on the complementary infrared and optical data, we identify ~ 186 young stellar objects in the observed area and extract five clusters within the dense ridge of F1. The calculated star formation rate (SFR) surface densities (Σ_{SFR}) in the clusters range from 1.4 to $2.5 M_\odot \text{Myr}^{-1} \text{pc}^{-2}$, with a mean value of $\sim 2.0 M_\odot \text{Myr}^{-1} \text{pc}^{-2}$. We therefore regard them as mini-starburst cluster candidates. The comparison between Σ_{SFR} and column density N_{gas} along the skeleton of F1 suggests that star formation is closely related to the dense gas in the cloud. Along the main filament F1, five bipolar outflows are also found. All these results indicate intense star-forming activities in the M120.1+3.0 molecular cloud.

Key words: ISM: clouds – ISM: jets and outflows – ISM: kinematics and dynamics – ISM: structure – stars: early-type

1. Introduction

Multi-wavelength surveys show that filaments are ubiquitous in molecular clouds (see, e.g., Schneider & Elmegreen 1979; Molinari et al. 2010; Yuan et al. 2021). Over the past decades, extensive studies have been conducted on various filaments, with lengths ranging from ~ 1 pc in the solar neighborhood (e.g., Arzoumanian et al. 2011; Hacar et al. 2013) up to ~ 100 pc in the Galactic plane (e.g., Jackson et al. 2010; Wang et al. 2014).

The Herschel Gould Belt Survey (HGBS; André et al. 2010) and Herschel infrared Galactic Plane Survey (Hi-GAL; Molinari et al. 2010) suggest an intimate connection between filaments and dense cores. André et al. (2010) found that the gravitationally bound cores are mostly located within thermally supercritical filaments, which have mass per unit length M_{line} larger than the critical value $M_{\text{line,crit}}$ and are generally believed to be unstable to radial collapse (Ostriker 1964). The observed velocity fields also reveal that the material around filaments is usually not static. Kirk et al. (2013) suggest that the longitudinal velocity gradients delineate the accretion process of gas material along the filaments, caused by local gravitational collapse

(see also Hacar & Tafalla 2011). The gas flows along filaments continuously bring fresh material into overdense regions and facilitate the process of star formation (Schneider et al. 2010; Hacar et al. 2017; Treviño-Morales et al. 2019; Li et al. 2022).

Most stars, probably all massive stars, are formed in clusters (Lada & Lada 2003; Krumholz et al. 2019). The numerical simulations support that clusters mainly form through hierarchical fragmentation of molecular clouds (see, e.g., Bonnell et al. 2003; Burkert & Hartmann 2004; Vázquez-Semadeni et al. 2019). The Spitzer surveys yielded an interesting result that the clusters are the local peaks of more extended sources that tend to follow the morphology of the filamentary molecular clouds (Allen et al. 2007; Gutermuth et al. 2009). Recently, the fragmentation of filaments into stars and clusters is also widely observed both in low-mass and high-mass star-forming regions (see, e.g., Hartmann 2002; Arzoumanian et al. 2013; Beuther et al. 2015; Zhang et al. 2015; Clarke et al. 2017). In a few filaments with high densities, there are even mini-starburst events occurring (e.g., Motte et al. 2003; Nguyen Luong et al. 2011; Willis et al. 2013). In order to better understand the role

filaments play in the process of star and cluster formation, it is of importance to investigate more filamentary molecular clouds and study the star formation activities therein.

The M120.1+3.0 molecular cloud, located in the Cep OB4 region, was first observed in ^{12}CO and $^{13}\text{CO } J=1-0$ emissions with the 4 m radio telescope of Nagoya University (Yang et al. 1990). It was named after its approximate Galactic coordinate. The cloud exhibited an S-shaped morphology and outflow activities. It is therefore an ideal target to study the relation between filaments and star formation.

In this paper, we conduct a detailed study on the M120.1+3.0 molecular cloud by combining the CO observations with complementary infrared (IR) and optical data. The CO data set is obtained as part of the Milky Way Imaging Scroll Painting (MWISP) project³, which is a large-scale unbiased survey of ^{12}CO , ^{13}CO and $\text{C}^{18}\text{O } J=1-0$ line emission toward the northern Galactic plane, conducted by the Purple Mountain Observatory (PMO) 13.7 m millimeter-wavelength telescope (Su et al. 2019; Sun et al. 2021). The IR and optical data are retrieved from Wide-field Infrared Survey Explorer (WISE), Two Micron All Sky Survey (2MASS) and Gaia surveys. The observations and data reduction are described in Section 2. In Section 3, we derive the basic physical properties of the cloud and present the results of identified filament structures, clumps and young stellar object (YSO) candidates. In Section 4, we discuss the relationship between filamentary structures and star-forming activities. The main conclusions are summarized in Section 5.

2. Observations and Data Reduction

2.1. PMO-13.7 m CO Observation

The observations toward the M120.1+3.0 cloud covered a region within $119^{\circ}3' \leq l \leq 121^{\circ}3'$ and $2^{\circ} \leq b \leq 4^{\circ}$, which were carried out with the PMO-13.7 m millimeter-wavelength telescope, located in Delingha, China, from 2013 March to 2016 July. As part of the MWISP project, the region was observed in the ^{12}CO , ^{13}CO and $\text{C}^{18}\text{O } J=1-0$ lines simultaneously with the nine-beam Superconducting Spectroscopic Array Receiver (SSAR; Shan et al. 2012). A Fast Fourier Transform Spectrometer (FFTS) was used as the back-end of the receiver, which has a total bandwidth of 1 GHz and contains 16,384 channels. The corresponding velocity resolution is 0.16 km s^{-1} for the ^{12}CO line and 0.17 km s^{-1} for the ^{13}CO and C^{18}O lines.

The observations were conducted in the position-switch on-the-fly (OTF) mode with a scanning rate of $50''$ per second and a dump time of 0.3 s. The spacing between the adjacent scanning was $15''$, which was able to fully sample the observed area. A specific local oscillator (LO) frequency was carefully selected so that the upper sideband was centered at

the ^{12}CO line and the lower sideband was able to cover the ^{13}CO and C^{18}O lines. The system temperatures were 191–387 K at the upper sideband, and 142–237 K at the lower sideband. In order to reduce the fluctuation of noise perpendicular to the scanning direction, each area was scanned in both longitude and latitude directions. The typical root mean square (rms) noise level was $\sim 0.5 \text{ K}$ for ^{12}CO and $\sim 0.3 \text{ K}$ for ^{13}CO and C^{18}O . The half power beamwidth of the telescope was about $52''$ at 115.2 GHz with the beam efficiency η_{MB} of 46%, and about $50''$ at 110.2 GHz with η_{MB} of 49%. More details about the telescope system are described in the telescope status report.⁴

The raw data were reduced by the GILDAS software.⁵ We eliminated abnormal data and then divided the survey data into $30' \times 30'$ FITS cubes. Finally, we mosaicked the data cubes of the M120.1+3.0 cloud to analyze the morphology and physical properties of molecular gas. All velocities given in this work are relative to the local standard of rest (LSR).

2.2. Complementary Infrared and Optical Data

WISE scanned the entire sky in four mid-IR bands W1, W2, W3 and W4, centered at 3.4, 4.6, 12 and $22 \mu\text{m}$, respectively (Wright et al. 2010). The AllWISE program (Cutri et al. 2013) combined the WISE images from different survey phases to form a more comprehensive view of the mid-IR sky. The beam sizes are $6''1$, $6''4$, $6''5$ and $12''0$ at the four observed bands W1–W4, respectively, with 5σ rms levels better than 0.08, 0.11, 1 and 6 mJy. We retrieved the WISE images and AllWISE catalog via the NASA/IPAC Infrared Science Archive.⁶ The AllWISE catalog also includes a match to the 2MASS data, which provide the observations at near-IR bands J ($1.25 \mu\text{m}$), H ($1.65 \mu\text{m}$) and K_s ($2.16 \mu\text{m}$) (Skrutskie et al. 2006).

The Gaia Early Data Release 3 (Gaia EDR3) catalog,⁷ as the first installment of Gaia Data Release 3, contains provisional astrometric parameters (position, parallax and proper motion) for more than 1.8 billion sources, with G -band (330–1050 nm) magnitudes ranging from 3 to 21 (Gaia Collaboration et al. 2021). In this work, we cross-match the YSO candidates with the EDR3 catalog and make use of the parallaxes to eliminate potential field stars. We also examine the proper motion to characterize the possible co-moving members.

3. Results

3.1. Overview of the M120.1+3.0 Molecular Cloud

Figure 1 shows the average spectra of the ^{12}CO , ^{13}CO and $\text{C}^{18}\text{O } J=1-0$ line emission toward the observed $2^{\circ} \times 2^{\circ}$

³ <http://www.radioast.nscd.cn/yhhjindex.php>

⁴ <http://www.radioast.nscd.cn/zhuanqitaibaogao.php>

⁵ <http://iram.fr/IRAMFR/GILDAS/>

⁶ <http://irsa.ipac.caltech.edu/frontpage/>

⁷ <https://www.cosmos.esa.int/gaia>

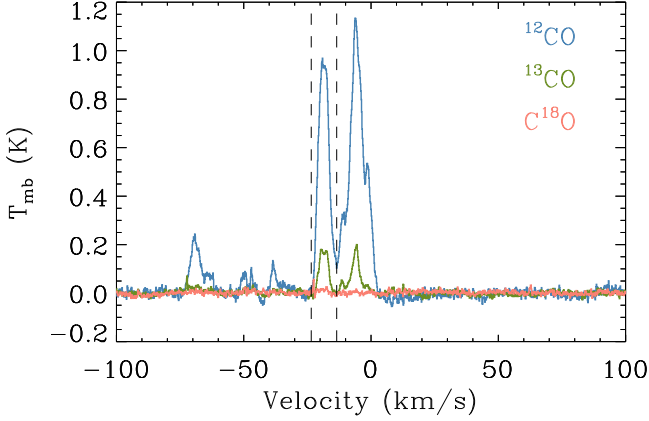


Figure 1. CO average spectra of the whole observed region ($2^\circ \times 2^\circ$). The blue, green and orange spectra represent ^{12}CO , ^{13}CO and C^{18}O $J = 1 - 0$ line emission, respectively. The dashed lines represent the velocity range ($-23.5 \sim -13.5 \text{ km s}^{-1}$) of the M120.1+3.0 molecular cloud (see Yang et al. 1990).

region of Cep OB4. The ^{12}CO average spectrum exhibits several velocity components. In this work, we focus on the velocity range from -23.5 to -13.5 km s^{-1} , which fully covers the emission of the M120.1+3.0 molecular cloud (see Yang et al. 1990). The other velocity components will be studied in future work.

Figures 2(a)–(c) presents the integrated intensity images of the ^{12}CO , ^{13}CO and C^{18}O emission, respectively. The ^{12}CO emission, as a tracer of diffuse gas, follows the overall morphology of the M120.1+3.0 molecular cloud. The emission map of ^{13}CO presents the denser part of the cloud, from which an S-shaped long filament and sub-filaments are revealed. The C^{18}O emission only appears at the densest part of the interior, which presents clumpy structure and is mainly located in the northwest of the cloud. Figure 2(d) features a three-color image of ^{12}CO and its isotopologues, with ^{12}CO in blue, ^{13}CO in green and C^{18}O in red for the M120.1+3.0 molecular cloud. As affirmed in this image, there are strong ^{12}CO emission, clear ^{13}CO emission and weak C^{18}O emission in this region.

The mean radial velocity of the cloud is roughly 19 km s^{-1} , which is similar to the velocity of the central region of Sh2-171. Thus, the distance of 850 pc was adopted for the M120.1+3.0 cloud, same as the Sh2-171 region (see Yang et al. 1990). In this work, we re-estimate a distance of 1.1 kpc for the M120.1+3.0 molecular cloud, using the Bayesian approach (Reid & Dame 2016) and the extinction method (Yan et al. 2019) (see Appendix A for details).

Based on the CO data, we rely on two methods to calculate the H_2 gas column densities and masses. In the first method, the column density is calculated under the assumption of local thermodynamic equilibrium (LTE). In order to obtain the excitation temperature, we assume that the ^{12}CO line emission

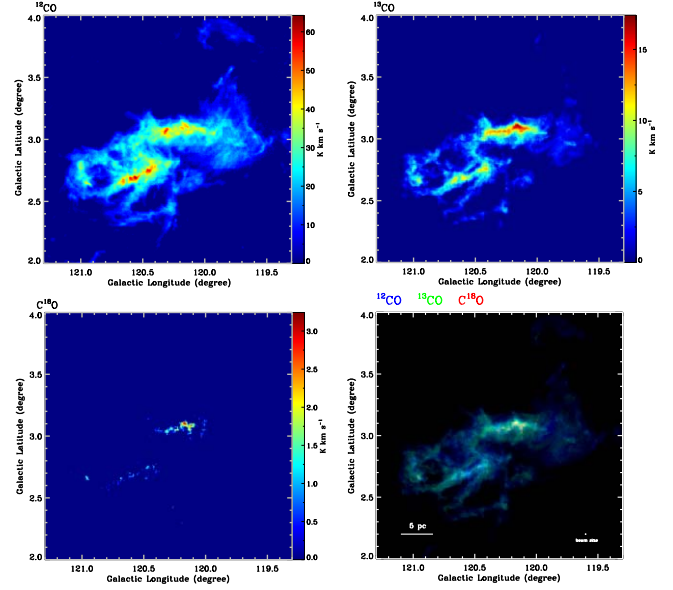


Figure 2. (a)–(c): Integrated intensity maps of ^{12}CO , ^{13}CO and C^{18}O . (d) Three-color image of ^{12}CO and its isotopologues. The blue color represents the integrated intensity of the ^{12}CO emission with velocity between -23.5 and -13.5 km s^{-1} (from (a)). The green color signifies the integrated intensity of ^{13}CO emission with velocity between -22 and -15 km s^{-1} (from (b)). The red color represents the integrated intensity of the C^{18}O emission with velocity between -21 and -17 km s^{-1} (from (c)).

is optically thick with the optical depth $\tau_{12} \gg 1$ and the beam filling factor is equal to unity. The excitation temperature T_{ex} can be calculated from the following formula

$$T_{\text{mb}} = [J(T_{\text{ex}}) - J(T_{\text{bg}})][1 - e^{(-\tau)}], \quad (1)$$

where T_{mb} is the main-beam brightness temperature, T_{bg} is the background temperature with the value of 2.7 K; $J_{\nu}(T) = T_0 / [e^{(h\nu/k_B T)} - 1]$, here $T_0 = h\nu/k_B$, k_B is the Boltzmann constant and h is the Planck constant. As seen in Figure 3, the excitation temperatures range from 3.2 to 16.5 K, with a mean value of ~ 9.9 K. Assuming that ^{13}CO and C^{18}O have the same excitation temperature with ^{12}CO , the optical depth of τ_{13} and τ_{18} can be derived as follows (Bourke et al. 1997):

$$\tau_{13} = -\ln \left[1 - \frac{T_{\text{mb}}(^{13}\text{CO})}{5.29} ([e^{5.29/T_{\text{ex}}} - 1]^{-1} - 0.164)^{-1} \right], \quad (2)$$

$$\tau_{18} = -\ln \left[1 - \frac{T_{\text{mb}}(\text{C}^{18}\text{O})}{5.27} ([e^{5.27/T_{\text{ex}}} - 1]^{-1} - 0.167)^{-1} \right]. \quad (3)$$

The mean values of the optical depth in the ^{13}CO and C^{18}O emission are 0.5 and 0.2, respectively. It is thus reasonable to assume that both ^{13}CO and C^{18}O emission are optically thin and derive the approximate column density expression (Bourke

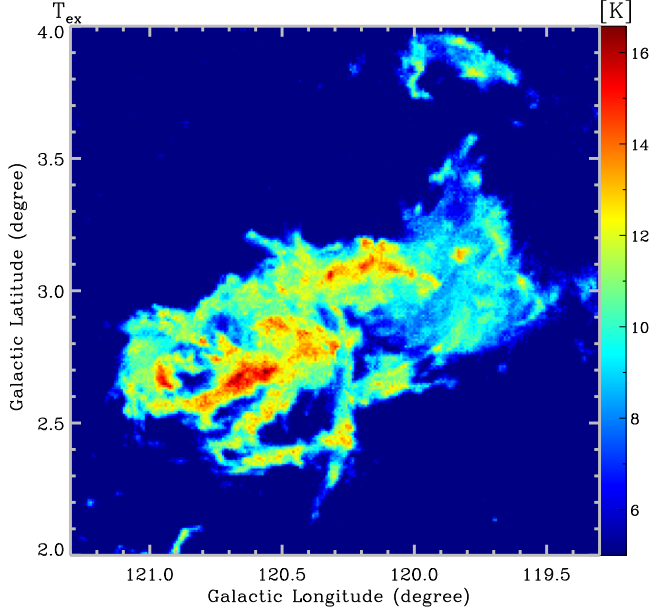


Figure 3. Excitation temperature map of the M120.1+3.0 molecular cloud, derived from the ^{12}CO emission (see the text).

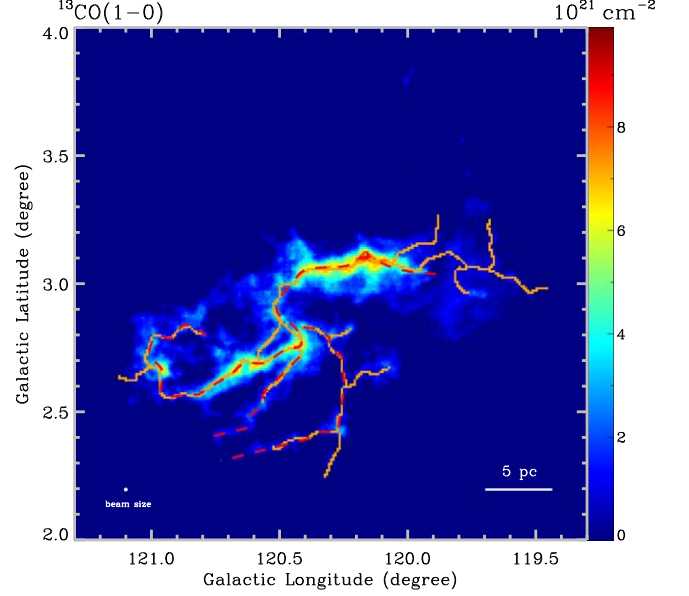


Figure 4. H_2 column density map derived from the ^{13}CO (1-0) emission. The solid orange lines trace the filaments identified by DisPerSE. The dashed red lines signify the filaments identified by combining the DisPerSE algorithm and visual inspection.

et al. 1997):

$$N(^{13}\text{CO}) = 2.42 \times 10^{14} \times \frac{\tau(^{13}\text{CO})}{1 - e^{-\tau(^{13}\text{CO})}} \frac{(1 + 0.88/T_{\text{ex}}) \times \int T_{\text{mb}}(^{13}\text{CO}) dV}{1 - e^{-T_0(^{13}\text{CO})/T_{\text{ex}}}}, \quad (4)$$

$$N(\text{C}^{18}\text{O}) = 2.54 \times 10^{14} \times \frac{\tau(\text{C}^{18}\text{O})}{1 - e^{-\tau(\text{C}^{18}\text{O})}} \frac{(1 + 0.88/T_{\text{ex}}) \times \int T_{\text{mb}}(\text{C}^{18}\text{O}) dV}{1 - e^{-T_0(\text{C}^{18}\text{O})/T_{\text{ex}}}}. \quad (5)$$

The abundance ratios of $[^{16}\text{O}/^{18}\text{O}] = 560$ (Wilson & Rood 1994), $\text{H}_2/^{12}\text{CO} \approx 1.1 \times 10^4$ (Frerking et al. 1982) and $[^{12}\text{C}/^{13}\text{C}] = 6.21D_{\text{GC}} + 18.71$ (Milam et al. 2005) are used to calculate the H_2 column density, where D_{GC} is the distance between the cloud and the Galactic center. The LTE mass of the molecular gas is calculated by

$$M = \mu m_{\text{H}} \int N(\text{H}_2) dS, \quad (6)$$

where μ is the mean molecular weight with the value of 2.83, m_{H} is the mass of a hydrogen atom and S is the area with CO emission.

In the second method, we calculate the H_2 gas column density by using CO-to- H_2 mass conversion factor X ,

$$N_{\text{H}_2} = X \int T_{\text{MB}, ^{12}\text{CO}} dV, \quad (7)$$

where $X = 2.0 \times 10^{20} \text{ cm}^{-2} \text{ K}^{-1} \text{ km}^{-1} \text{ s}$ (Bolatto et al. 2013).

The estimated mass of this cloud is about $3.1 \times 10^4 M_{\odot}$ from ^{12}CO (X-factor), $1.2 \times 10^4 M_{\odot}$ from ^{13}CO (LTE) and $7.8 \times 10^3 M_{\odot}$ from C^{18}O (LTE).

3.2. Structures and Properties of Filaments

Based on the column density calculated from ^{13}CO emission, we apply the Discrete Persistent Structure Extractor (DisPerSE) algorithm (Sousbie 2011) to search for filamentary structures. DisPerSE is an algorithm designed to extract the persistent structures from astrophysical data sets by connecting the topologically critical points (e.g., maximum and minimum points and saddle points). In a parameter setting, it is important to balance the persistence and robustness thresholds. We set the persistence threshold as 1.0×10^{21} ($\sim 6 \times \text{rms}$) and the robustness threshold as 2.0×10^{21} (see the DisPerSE⁸ website for more details). The solid orange lines in Figure 4 trace the filaments identified by DisPerSE.

The results obtained by the DisPerSE algorithm are objective. However, since the algorithm extracts filamentary structures on a 2D diagram, it fails in analyzing the velocity distributions. Thus, we further check the filament structures with visual inspection, according to the spatial distribution and velocity structure. In Figure 5, we present the ^{12}CO velocity channel map with ^{13}CO contours overlaid to check the spatial distribution of the filament structures. Figure 6 depicts the

⁸ <http://www2.iap.fr/users/sousbie/web/html/index55a0.html?category/Quick-start>

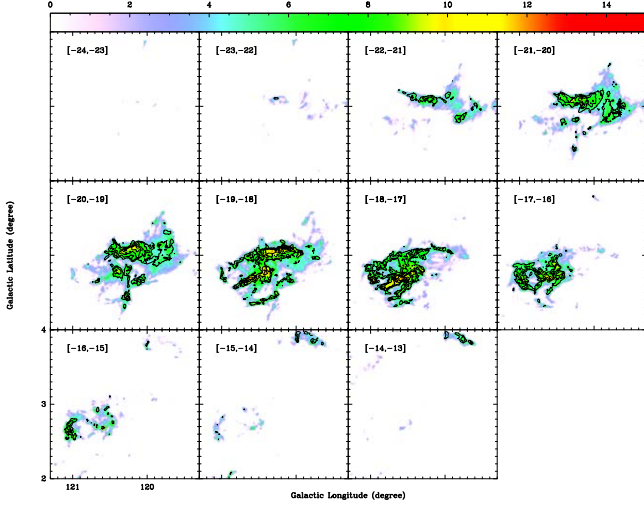


Figure 5. Velocity channel maps of the ^{12}CO (1-0) emission. The unit of the scale bar is K km s^{-1} . The integrated velocity range (km s^{-1}) is marked in the top left corner of each panel. The contours represent the ^{13}CO (1-0) emission. In each panel, contour levels start at 3σ and increase with a step of 5σ ($\sigma \sim 0.25 \text{ K km s}^{-1}$).

^{13}CO velocity distribution, with different colors representing different velocity components. We remove the discontinuous structures in space or velocity, the structures with width less than the beam size ($51''$, $\sim 0.27 \text{ pc}$ in the distance of 1.1 kpc) and the structures with length-to-width ratio less than 5 (the widths are calculated in the following text). By combining the DisPerSE algorithm and visual inspection, we identify three filaments in the M120.1+3.0 molecular cloud. We name the strongest filament with C^{18}O emission (see Figure 2(c)) the main filament F1, and the other two are sub-filaments F2 and F3, respectively. We plot the identified filament trails in Figures 4 and 6. From these maps, we can clearly see that the M120.1+3.0 molecular cloud presents a “hub-filament” structure, which consists of a long S-shaped main filament F1 and two sub-filaments F2 and F3. Along the direction of the arrow line in Figure 6, we extract the ^{13}CO position–velocity (PV) diagram of the main filament F1, which is shown in Figure 7. We note that the main filament F1 presents many sharp spur structures and clumpy positions with obvious velocity differences, which will be analyzed in detail in the discussion section.

We adopt the same method as described in Arzoumanian et al. (2011) to derive the mean radial density profile of each filament. We first extract the skeletons (the dashed red lines in Figure 4) of filaments on the H_2 column density map, and then compute the tangential direction of each pixel along the skeletons. Finally, the column density profiles perpendicular to the tangent of each pixel are obtained. We average all the column density profiles along each filament to derive their mean radial density profiles, which are displayed in Figure 8.

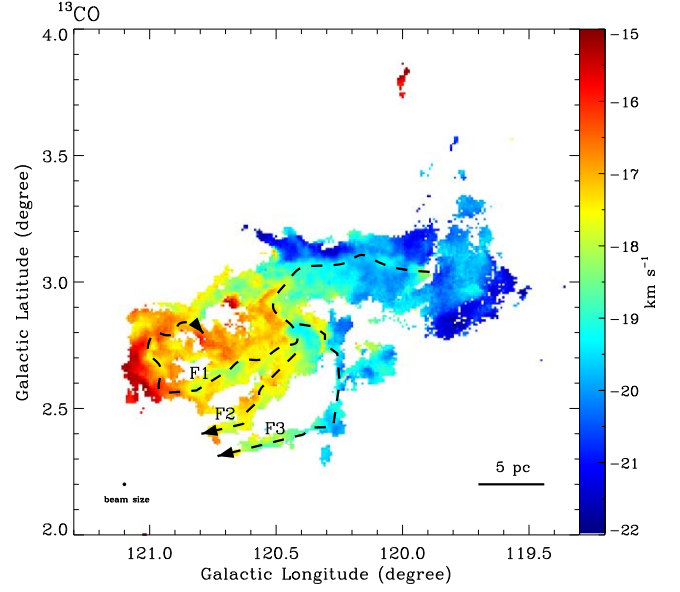


Figure 6. Velocity distribution map calculated from the ^{13}CO (1-0) emission. The velocity range is from -22 to -15 km s^{-1} . The dashed black lines correspond to the identified filaments.

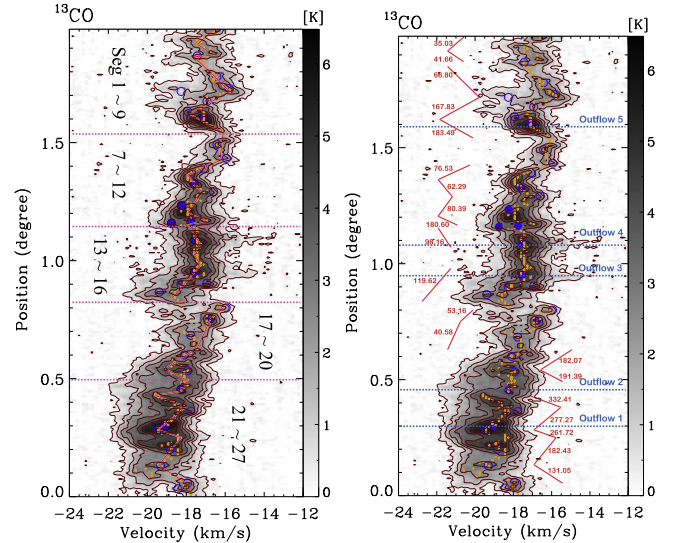


Figure 7. ^{13}CO (1-0) PV maps along the direction of the main filament F1. The contour levels start at 3σ and increase with a step of 6σ ($\sigma \sim 0.15 \text{ K}$). The filled and open blue circles represent virialized and unvirialized clumps, respectively. (Left) The orange points mark the positions of peak emissions. The red lines represent the adjusted fitting lines and the segment numbers increase from top to bottom. (Right) The red lines present the selected segments with the estimated accretion rates ($\alpha = 45^\circ$) in the unit of $M_\odot \text{ Myr}^{-1}$ labeled nearby (see Section 4.1). The dotted blue lines trace the positions of outflows identified in Section 4.4.

The dashed red lines are the results of Gaussian fitting, from which we estimate the full width at half maximum (FWHM) width of each filament (see Table 1). The measured FWHM widths of our sample are between 0.9 – 1.7 pc , which

Table 1
Properties of Filaments

Filament	Length (pc)	Width (pc)	T_{ex} (K)	$N_{\text{H}_2}(^{13}\text{CO})$ (10^{21} cm^{-2})	Δv (km s^{-1})	c_s (km s^{-1})	σ_{NT} (km s^{-1})	σ_{tot} (km s^{-1})	M_{LTE} (M_{\odot})	M/L ($M_{\odot} \text{ pc}^{-1}$)	M_{crit} ($M_{\odot} \text{ pc}^{-1}$)
F1	39.43	1.70	12.04	2.32	1.67	0.187	0.708	0.732	3600	91	16.30
F2	8.96	0.91	11.51	1.07	0.94	0.183	0.396	0.434	220	25	15.59
F3	19.47	0.96	10.64	0.45	0.94	0.176	0.395	0.433	207	13	14.42

Note. Properties of the identified filaments. Columns 2–5 are the length, width, excitation temperature and mean H_2 column density traced by ^{13}CO . Columns 6–9 are the linewidth, thermal velocity dispersion, non-thermal velocity dispersion and total velocity dispersion respectively. Columns 10–12 are the LTE mass, linear mass and critical line mass of each filament respectively.

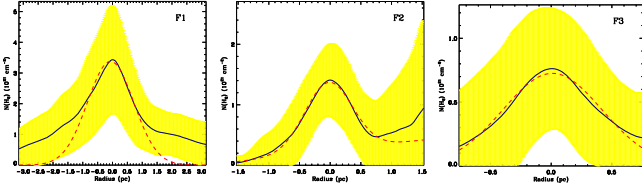


Figure 8. Mean radial column density profiles (blue lines) perpendicular to the identified filaments. The yellow areas show the dispersion of the radial profiles with the value of $\pm 1\sigma$. The dashed red curves follow the Gaussian fittings to the inner part of the profiles.

are similar to the results derived from the MWISP surveys (e.g., Xiong et al. 2017, 2019). Arzoumanian et al. (2011) suggested that the filament width has a typical value of ~ 0.1 pc based on the Herschel observations (but see also Panopoulou et al. 2022). Whereafter, with higher-resolution observations from Atacama Large Millimeter/submillimeter Array (ALMA), Hacar et al. (2018) identified 55 fiber structures with a median FWHM width of 0.035 pc in Orion. Since the dust emission observed by Herschel traces denser regions than the CO emission in our observations, and the angular resolution in our survey is $51''$ (or ~ 0.27 pc at a distance of 1.1 kpc), our results are reasonable. The mean excitation temperature, column density and the mass per unit length (M_{line}) of each filament are computed and listed in Table 1.

3.3. Clumps in the Cloud

We use the GaussClumps algorithm in the GILDAS package to identify molecular clumps with the ^{13}CO data cube (Stutzki & Guesten 1990). The algorithm assumes that the density distribution of each clump is Gaussian-shaped both in spatial and velocity coordinates. By implementing an interactive subtraction method, the GaussClumps procedure decomposes integral intensity distribution into the individual Gaussian-shaped clumps. This process will continue until the peak intensity of the residual map reaches the lowest level, which is determined by the parameter THRESHOLD. We set

the parameter THRESHOLD as 2.25 K ($\sim 9 \times \text{rms}$). When the procedure is finished, partial physical parameters of clumps are given in the output file, such as position coordinate, LSR velocity, linewidth, etc. We remove the clumps with pixels beyond the edge of the map, the clumps with short axis less than the angular resolution ($51''$) and the clumps with the ratio of major axis to minor axis larger than 3. Eventually, approximately 150 ^{13}CO clumps are identified. In Figure 9, we present the distribution of the clumps on the ^{13}CO integrated intensity map. More than 50% of clumps are located within the FWHM width of filaments (see width values in Table 1). We further calculate the effective radius, LTE mass and volume density for each clump. The effective radius is calculated as follows

$$R_{\text{eff}} = \frac{1}{2}D(\theta_a\theta_b - \theta_{\text{mb}}^2)^{1/2}, \quad (8)$$

where D is the distance of the cloud and θ_{mb} is the main beamwidth of the telescope. θ_a and θ_b are the fitted clump sizes. The LTE mass and volume density of each clump are then derived with the formulas $M = \mu m_{\text{H}} N(\text{H}_2) \times \pi R_{\text{eff}}^2$ and $n(\text{H}_2) = M / (\frac{4}{3}\pi R_{\text{eff}}^3 \mu m_{\text{H}})$, respectively.

The linewidth $\Delta\nu_{\text{FWHM}}$ listed in the outfile is the observed linewidth. The thermal portion of the linewidth is $\Delta\nu_{\text{th}} = \sqrt{8 \ln 2 \times k_{\text{B}} T_{\text{kin}} / m}$, where T_{kin} is the kinetic temperature and m is the mean molecular mass. The non-thermal portion is calculated by $\Delta\nu_{\text{nth}} = \sqrt{\Delta\nu_{\text{FWHM}}^2 - \Delta\nu_{\text{th}}^2}$. We then derive the thermal (c_s) and non-thermal (σ_{NT}) velocity dispersions, which are listed in Table B1. We note that σ_{NT} values are significantly larger than c_s for all clumps, indicating that non-thermal broadening mechanisms are dominant in the clumps. Figure 10 features the distributions of the clump size, excitation temperature and volume density, with the median value labeled on each panel.

3.4. Sample of Young Stellar Object Candidates

We extract a YSO sample from the AllWISE point-source catalog, which contains mid-IR data from the WISE survey and

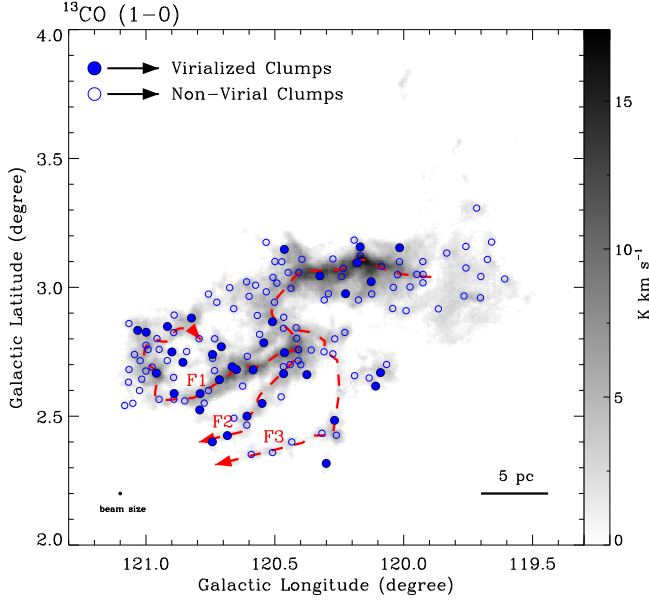


Figure 9. Distribution of identified ^{13}CO clumps (circles) on the ^{13}CO integrated intensity map (panel b in Figure 2). The filled circles represent virialized clumps ($\alpha_{\text{vir}} < 2$). The open circles signify unvirialized clumps. The dashed red lines trace the identified filaments.

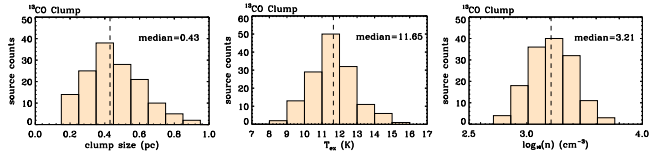


Figure 10. Statistics of size (left), excitation temperature (middle) and volume density (right) of the ^{13}CO clumps in the M120.1+3.0 cloud. The median value is marked on the top right of each panel.

a match to the near-IR data in the 2MASS catalog (Cutri et al. 2013). We select the area within $119^{\circ}5 \leq l \leq 121^{\circ}2$ and $2^{\circ}3 \leq b \leq 3^{\circ}4$, which encloses the whole molecular cloud of interest in projection, to identify YSO candidates. Since Class III YSOs have already disrupted their envelope and disk, we can scarcely separate them from main sequence stars by only using IR data. Thus, we only focus on the IR-excess sources (i.e., Class I & Class II objects) in this text. The main part of the YSO sample is extracted by applying the same scheme as described in Koenig & Leisawitz (2014, hereafter KL14). First, we eliminate the contaminants from star-forming galaxies (SFG) and active galactic nuclei (AGNs) (see Figure 11(a) and (b)). After that, we identify and classify the YSO candidates either in the WISE color-color and color-magnitude diagrams or the diagrams combined with the 2MASS bands, which are shown in Figure 11(c) and (d). In the end, we reject the asymptotic giant branch (AGB) and Classical Be (CBe) stars

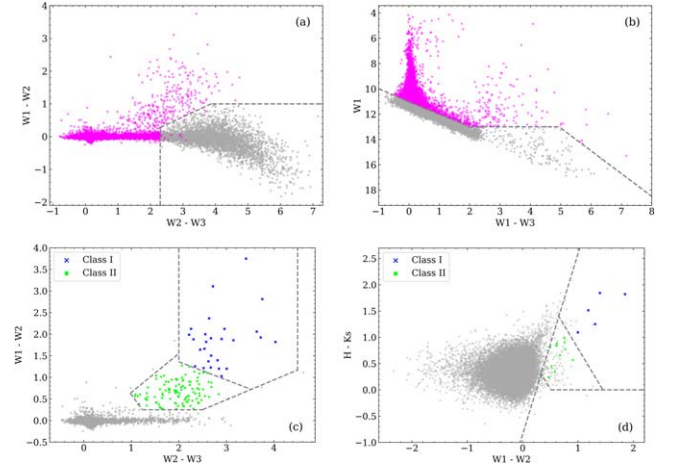


Figure 11. Color-color and color-magnitude diagrams of AllWISE sources in the area of the M120.1+3.0 cloud. (a) Removing the SFG (gray dots). (b) Removing the AGNs (gray dots). (c) The selection and classification of YSOs with WISE data. (d) The selection and classification of YSOs with WISE-2MASS data. The dashed lines represent the criteria proposed in Koenig & Leisawitz (2014).

for all the YSO candidates selected from the previous steps and then there are 107 sources left as the final KL14 sample (see KL14 for more details on the YSO Finding Scheme).

As a supplement, we select additional YSO candidates from the $K_s - W1$ versus $K_s - W2$ and $H - K_s$ versus $H - W2$ color-color diagrams (hereafter KW12 and HKW, respectively). To minimize the contamination of extended emission, we adopt a set of data quality screening criteria to the bands used in each color-color space before YSO selection:

$$\begin{aligned}
 w1\text{snr}, w2\text{snr} &> 10 \\
 w1_sigmpro &< 0.2\text{mag}, w2_sigmpro < 0.2\text{mag} \\
 w1\text{rchi} &< 20, w2\text{rchi} < 20 \\
 h_sig, k_sig &< 0.2\text{mag}.
 \end{aligned} \tag{9}$$

These conditions are set by referring to the description of AllWISE parameters on the official website.⁹

1. For the KW12 selection scheme, we adopt the following criteria to select the YSO candidates:

$$\begin{aligned}
 K - W1 &\leq 0.75 \times (K - W2) - 0.0725 \\
 K - W2 &\geq 1.1 \\
 \text{and} \\
 (K - W1) + \sqrt{K_{\text{err}}^2 + W1_{\text{err}}^2} &\leq 0.75 \\
 \times (K - W2) - 0.0725.
 \end{aligned} \tag{10}$$

⁹ https://wise2.ipac.caltech.edu/docs/release/allwise/expsup/sec2_1a.html

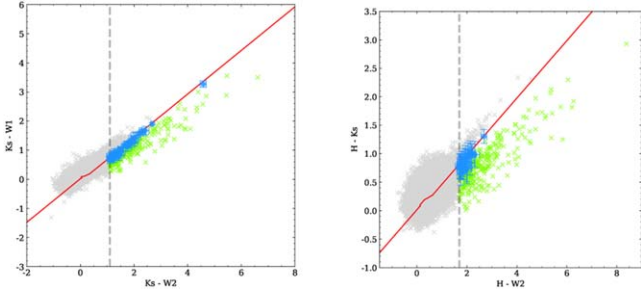


Figure 12. Two color–color YSO selection diagrams (KW12 and HKW). The segmented red lines represent the intrinsic colors of early-type dwarfs (Pecaut & Mamajek 2013) and reddening vectors (Wang & Chen 2019). The dashed gray lines are the cut-off borders and the gray crosses show the sources filtered out by the first two selection criteria in Equations (10) and (11). The green crosses represent the YSO candidates and the blue dots with error bars correspond to the sources that are removed under the consideration of photometric uncertainties.

2. For the HKW selection scheme, the selection criteria are:

$$\begin{aligned}
 H - K &\leq 0.505 \times (H - W2) - 0.043 \\
 H - W2 &\geq 1.7 \\
 &\text{and} \\
 (H - K) + \sqrt{H_{\text{err}}^2 + K_{\text{err}}^2} &\leq 0.505 \\
 &\times (H - W2) - 0.043,
 \end{aligned} \tag{11}$$

where 0.75 and 0.505 represent the slope of the extinction vector in KW12 and HKW spaces respectively, and the extinction law we adopted here is from Wang & Chen (2019). The extinction of YSO is either from the circumstellar disk or from foreground interstellar medium (ISM), or both. Thus, the first criterion for each scheme is set to avert the mixture of the embedded early-type main sequence stars and the YSO sample. The second criterion is set to separate out the sources with significant IR-excess. In order to further reduce the contamination, we take the photometric error into account and apply the last selection criterion to filter the YSO candidates strictly. The KW12 and HKW selection diagrams are displayed in Figure 12 and the green dots represent the YSOs selected as the second sample. We test these two color–color methods with the YSO samples in the Orion (Megeath et al. 2016) and Perseus (Wang et al. 2022) region, and find that the two methods can effectively isolate a YSO with IR-excess, with only less than $\sim 5\%$ diskless sources mixing in.

We combine the YSO samples extracted in different schemes (KL14, KW12 and HKW) and cross-match all the YSO candidates with Gaia EDR3 data (Gaia Collaboration et al. 2021). The closest Gaia source within a $2''$ radius is thought to be associated with the AllWISE object. For the sources with Gaia parallax $\text{plx} > 0$ and renormalized unit weight errors $\text{RUWE} < 1.4$, we compute their distances and

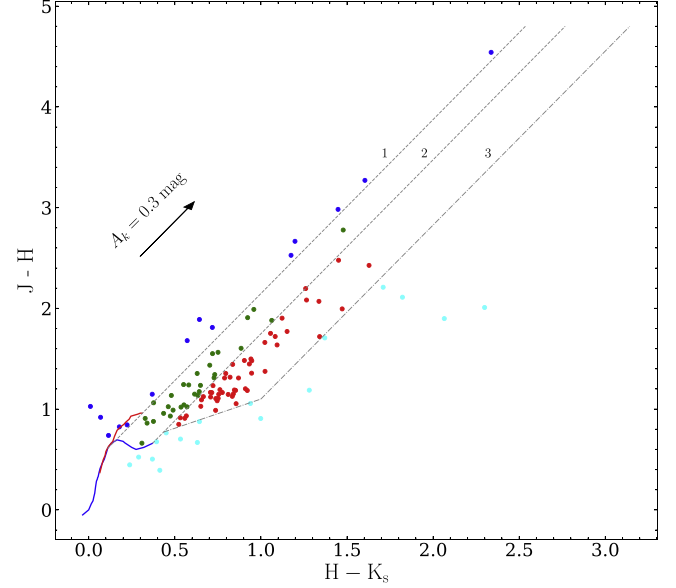


Figure 13. $H - K_s$ vs. $J - H$ color–color diagram. The solid blue and red lines represent the intrinsic color of M6 to B8 dwarfs and M7 to G0 giants, respectively (Bessell & Brett 1988). The arrow is the reddening vector and the two dashed lines are parallel to it (Flaherty et al. 2007). The dash–dotted lines indicate the tracks of T Tauri stars (Meyer et al. 1997). The dots with different colors represent the YSO candidates in different regions, and their extinction values are computed with different methods (Fang et al. 2013a).

consider the sources with distance range from ~ 950 to 1250 pc related to the cloud, which has the distance of ~ 1.1 kpc. The YSO catalogs with and without distances are listed in Tables B2 and B3, respectively, with a total of 186 sources. For sources that have detections in 2MASS J , H and K_s bands, we calculate their extinction in the $H - K_s$ versus $J - H$ color–color diagram (Bessell & Brett 1988), using the same method as described in Fang et al. (2013a). The extinction law from Wang & Chen (2019) is adopted to convert color excess $E(J - H)$ to A_v for sources in Regions 1, 2 and 3 (see Figure 13). The mean value of A_v is estimated to be ~ 6 mag, which may explain why only 13% of sources in our sample have Gaia distance. Since most IR-excess sources are at a very early stage of evolution and embedded deeply in the molecular cloud, they are usually invisible in optical band. We then make the RGB map with WISE data and superimpose YSO candidates to check the reliability of our sample. Figure 14 confirms that most YSO candidates are located within the molecular cloud. Also, the majority of the point sources with bright W3 and W4 photometry are well identified. Even so, it is hard to say that all the sources we identified are bona fide YSOs. We still need the spectroscopic observations to further confirm the YSO sample.

For the sources in Table B3 (i.e., the sources with Gaia counterparts), we further exhibit their proper motion distribution. The red ellipse in Figure 15 represents the 1σ confidence ellipse centered on the mean values (except one extreme case

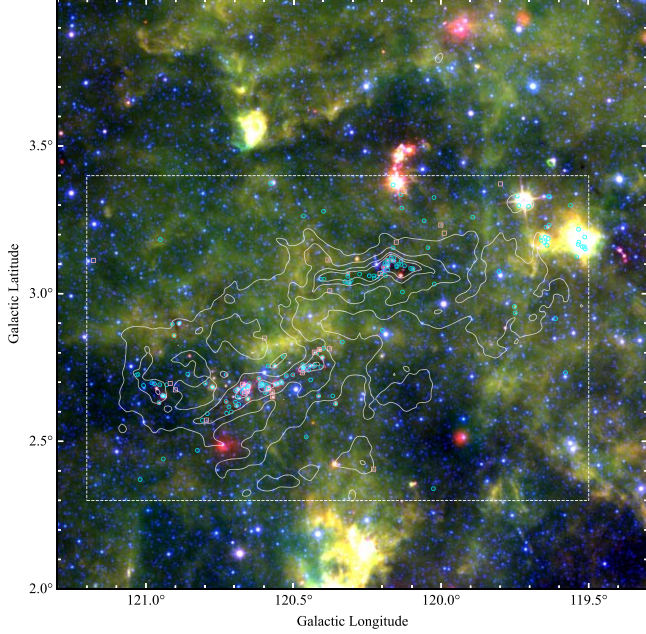


Figure 14. Three-color image of WISE bands (blue = $4.6 \mu\text{m}$, green = $12 \mu\text{m}$, red = $22 \mu\text{m}$). The white box shows the area selected for YSO searching. The contours exhibit the ^{13}CO emission (Figure 2(b)) with levels at 1, 5, 9 and 11 K km s^{-1} ($\sigma \sim 0.27 \text{ K km s}^{-1}$). The cyan circles and pink squares represent YSOs with and without distance, respectively.

with $\mu_\alpha \cos \sigma > 6 \text{ mas yr}^{-1}$) of the proper motions ($\mu_\alpha \cos \sigma$, μ_σ). We treat 21 sources within the ellipse as co-moving population candidates, which are labeled with “c” in the column “Gaia EDR3” in Table B3. We note that the three YSOs outside the ellipse are located further away from the molecular cloud than the co-moving members (the blue triangles in Figure 18).

4. Discussion

4.1. Gas Kinematics of the Filaments

Both numerical simulation and theoretical calculation suggest that filaments with gravitational instability will fragment into star-forming cores (Nagasawa 1987; Samal et al. 2015). Rotation and magnetic field in filaments may prevent fragmentation, but they hardly affect the length and mass scales involved (Larson 1985). Similar to cylinders, self-gravitating and isothermal filaments also have their own critical equilibrium masses M_{crit} . When line masses M_{line} of filaments exceed critical equilibrium masses M_{crit} , filaments are in a thermally supercritical state, which will be gravitationally unstable to collapse radially and subject to fragmentation along the length (e.g., Inutsuka & Miyama 1997). The thermally subcritical filaments with $M_{\text{line}} < M_{\text{crit}}$ may be expected to disperse, unless external pressure is provided to confine them. The critical line mass of the unmagnetized isothermal cylinder

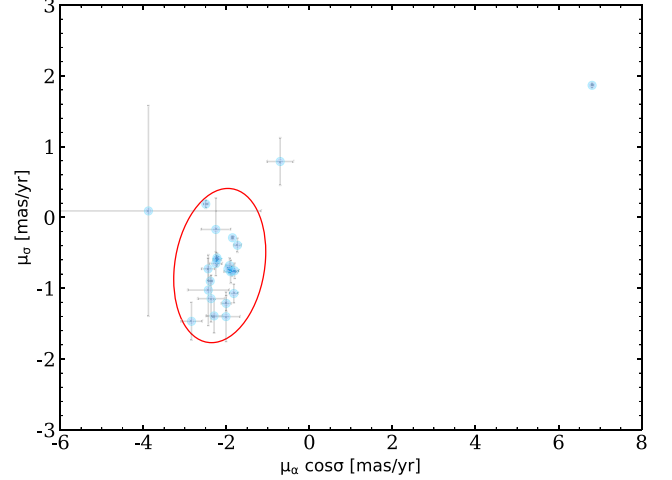


Figure 15. Proper motion diagram of the YSO candidates in Table B3. The red ellipse shows the 1σ confidence ellipse, which is centered on the median of the proper motions.

can be described in the following form (Ostriker 1964)

$$M_{\text{crit}} = \frac{2k_{\text{B}}T_{\text{kin}}}{\mu m_{\text{H}}G}, \quad (12)$$

where T_{kin} is the kinetic temperature derived from T_{ex} assuming gas densities greater than the effective critical density of the $^{12}\text{CO } J=1-0$ transition and $\sqrt{\frac{k_{\text{B}}T_{\text{kin}}}{\mu m_{\text{H}}}} = c_{\text{s}}$ is the local thermal sound speed. The gravitational constant G has the value of $1/232 \text{ km}^2 \text{ s}^{-2} M_{\odot}^{-1} \text{ pc}$ (Solomon et al. 1987). Therefore, the critical line mass is only determined by the value of the excitation temperature.

The median excitation temperature of the filaments in the M120.1+3.0 cloud is in the range between 10 and 13 K. Using the excitation temperature listed in Table 1, we calculate the critical linear masses, which are 16.30, 15.59 and $14.42 M_{\odot} \text{ pc}^{-1}$ for filaments F1, F2 and F3, respectively. Filaments F1 and F2 are thermally supercritical filaments with their observed linear masses (see Table 1) significantly higher than the critical line masses. The observed linear mass ($13 M_{\odot} \text{ pc}^{-1}$) of filament F3 is slightly smaller than its critical line mass ($14.42 M_{\odot} \text{ pc}^{-1}$). André et al. (2010) suggested that only thermally supercritical filaments can produce prestellar cores and exhibit evidence of star formation activities. Given that only one virialized clump is found in filament F3 (see Figure 9), we consider filament F3 as a thermally subcritical filament.

Unlike the case of F3, the main filament F1 is associated with a number of virialized clumps (see Section 4.2) and presents clear localized systematic motions in the ^{13}CO PV diagram (see Figure 7). Similar PV diagrams have been reported in other observations, such as the Serpens South (Kirk et al. 2013), OMC-1 (Hacar et al. 2017), G350.5 (Liu et al. 2019) and California (Guo et al. 2021) clouds. Kirk et al. (2013) suggested

that the longitudinal velocity gradient provides good evidence for the converging of material flow along the filament toward local clumps. Filament F1 is therefore a good sample to analyze the kinematics of supersonic filaments. We first extract the point of peak emission at each position from the PV diagram and then fit the points of different segments with a simple linear form. The results are shown in Figure 7. Note that the segments and fitted lines also have been adjusted according to the morphology of contours. We calculate the lengths, velocity differences and masses for all segments. Considering the distance of the cloud and the resolution of the telescope, we choose the segments with velocity difference larger than 0.5 km s^{-1} ($\sim 3 \times$ velocity resolution) and length larger than 0.56 pc ($\sim 2 \times$ beam at 1.1 kpc) to estimate the accretion rates. The accretion rate along the filament is given by $\dot{M} = \frac{dv}{dr} \times \frac{M}{\tan(\alpha)}$, where $\frac{dv}{dr}$ represents the velocity gradient and α is the inclination angle between F1 and the plane of the sky (see the details in Kirk et al. 2013). We calculate the accretion rates under the assumption of $\alpha = 30^\circ, 45^\circ, 60^\circ$. The results are listed in Table 2. As $\alpha = 45^\circ$, the accretion rates in F1 range from 35 to $332 M_\odot \text{ Myr}^{-1}$ with a mean value of $\sim 132 M_\odot \text{ Myr}^{-1}$, which is comparable to the results of IRDC G035.39-00.33 ($\sim 70 \pm 40 M_\odot \text{ Myr}^{-1}$, Henshaw et al. 2014), OMC-1 ($\sim 55 M_\odot \text{ Myr}^{-1}$, Hacar et al. 2017) and the cluster LkH α 101 region in the California cloud ($\sim 101 M_\odot \text{ Myr}^{-1}$, Guo et al. 2021). We mark the positions of outflows (see Section 4.4) and the clumps with distance from the skeleton of F1 less than the median of the effective radius ($\sim 80''$) of all clumps (see Figure 10(a)). We note that high-accretion rates occur in the outflow regions, which may support the perspective that outflows are intimately related to the accretion process (Shu et al. 2000).

In order to further analyze the internal dynamical state of filaments, it is also necessary to calculate the line of sight (l.o.s.) non-thermal velocity dispersion (e.g., Hacar & Tafalla 2011; Hacar et al. 2018). The non-thermal velocity dispersion σ_{NT} can be calculated with the following formula:

$$\sigma_{\text{NT}} = [\sigma_{\text{obs}}^2 - \sigma_{\text{obs}, T}^2]^{1/2}, \quad (13)$$

where the observed velocity dispersion is obtained from the equation $\sigma_{\text{obs}} = \Delta v / \sqrt{8 \ln 2}$ and Δv is the measured FWHM linewidth of the observed spectra. The observed thermal velocity dispersion is described as $\sigma_{\text{obs}, T} = \sqrt{\frac{k_B T}{\mu_{\text{obs}} m_{\text{H}}}}$ and μ_{obs} is the molecular weight of emitting species; $\mu_{\text{obs}} = 29$ for ^{13}CO . The calculated results are listed in Table 1. The ratio of $\sigma_{\text{NT}}/c_s(T)$ is often used to estimate whether the observed filaments are subsonic ($\sigma_{\text{NT}}/c_s(T) \leq 1$), transonic ($1 < \sigma_{\text{NT}}/c_s(T) \leq 2$) or supersonic ($\sigma_{\text{NT}}/c_s(T) > 2$) (Hacar et al. 2018). We note that all the three filaments are supersonic with the ratio of $\sigma_{\text{NT}}/c_s(T) > 2$. Therefore, additional support provided by non-thermal motions cannot be neglected. Arzoumanian et al.

Table 2
Properties of Segments

Segments	ΔL	ΔV	M_{LTE}	$\dot{M} (30^\circ)$	$\dot{M} (45^\circ)$	$\dot{M} (60^\circ)$
	(pc)	(km s^{-1})	(M_\odot)	($M_\odot \text{ Myr}^{-1}$)	($M_\odot \text{ Myr}^{-1}$)	($M_\odot \text{ Myr}^{-1}$)
Seg1	1.36	1.00	46.79	60.67	35.03	20.22
Seg2	0.88	0.83	43.20	72.16	41.66	24.05
Seg3	0.40	0.83	19.45
Seg4	2.56	1.66	100.78	115.70	66.80	38.57
Seg5	1.82	2.08	144.00	290.69	167.83	96.90
Seg6	1.54	1.74	158.58	317.81	183.49	105.94
Seg7	2.24	0.17	59.52
Seg8	1.20	1.66	54.12	132.55	76.53	44.18
Seg9	1.60	0.66	106.59	78.34	45.23	26.11
Seg10	1.44	0.66	218.43	178.30	102.94	59.43
Seg11	0.72	1.00	127.71	312.81	180.60	104.27
Seg12	0.24	1.00	46.38
Seg13	1.60	0.66	231.38	170.02	98.16	56.67
Seg14	0.80	0.33	92.63
Seg15	0.96	0.33	92.46
Seg16	2.72	1.50	213.05	207.19	119.62	69.06
Seg17	0.96	0.66	75.18	92.08	53.16	30.69
Seg18	2.32	0.66	138.73	70.28	40.58	23.43
Seg19	1.68	1.66	180.26	315.35	182.07	105.12
Seg20	0.96	1.16	154.70	331.50	191.39	110.50
Seg21	0.88	0.33	151.72
Seg22	0.32	1.33	79.31
Seg23	0.93	1.58	191.54	575.75	332.41	191.92
Seg24	1.87	1.41	359.71	480.25	277.27	160.08
Seg25	0.64	1.16	140.99	453.31	261.72	151.10
Seg26	2.24	1.16	344.04	315.97	182.43	105.33
Seg27	1.52	1.49	130.43	226.99	131.05	75.66

Note. Properties of the identified segments along the main filament F1. Column 1 is the segment number, which increases from top to bottom along the PV diagram of F1. Columns 2–4 are the length, velocity gradient and mass respectively. Columns 5–7 are the accretion rates with different inclination angles ($\alpha = 30^\circ, 45^\circ, 60^\circ$, respectively).

(2013) suggested that the high velocity dispersions of supersonic filaments may be caused by gravitational contraction, but not caused by supersonic interstellar turbulence. In the M120.1 +3.0 cloud, we find that there are many virial clumps distributed along filaments F1 and F2. We consider that local collapse in the filaments may be one of the reasons for increasing the total velocity dispersion. In addition, we also note that there are YSOs and outflows distributed along the main filament F1, which are shown in Sections 4.3 and 4.4. Hence, we consider that star-forming activity in the filaments (e.g., outflow, accretion) is another reason for large velocity dispersion.

4.2. Gravitational Stability of Clumps

The observed results from Herschel surveys indicate that compact filaments will fragment into prestellar cores (e.g., André et al. 2010; Palmeirim et al. 2013), which is consistent

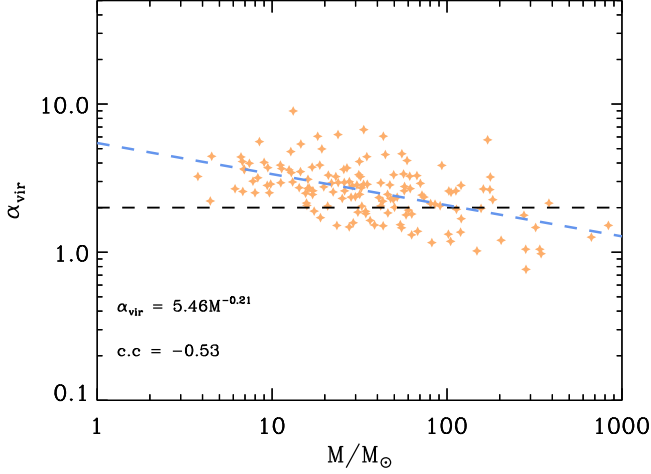


Figure 16. The relationship between virial parameter α_{vir} and clump mass M_{LTE} . The horizontal dashed black line at $\alpha_{\text{vir}} = 2$ gives the lowest critical virial parameter for non-magnetized clumps. The dashed blue line delineates the result of a linear least-squares fitting to clumps.

with numerical simulations (e.g., Mac Low & Klessen 2004). Thus, further study of the clumps will help us to understand the evolution of interstellar filaments and their role in the star formation process. The virial mass of each clump can be calculated as (Solomon et al. 1987; Evans 1999),

$$M_{\text{vir}} = 209R_{\text{eff}} \times \Delta\nu_{\text{FWHM}}^2, \quad (14)$$

where $\Delta\nu_{\text{FWHM}}$ is the linewidth of the ^{13}CO clump. The virial parameter $\alpha_{\text{vir}} = \frac{M_{\text{vir}}}{M_{\text{LTE}}}$, which is defined as the ratio of virial mass to LTE mass, is used to investigate whether a clump is subcritical or supercritical. The results of our sample are listed in Table B1.

For a non-magnetized sphere, Ebert (1955) and Bonnor (1956) gave the critical virial parameter $\alpha_{\text{vir}} \approx 2$ as the lowest critical value. The clumps with $\alpha_{\text{vir}} < 2$ are gravitationally bound and may collapse to form stars, while the clumps with higher α_{vir} may be in the expanding state, unless external pressure is supplied. In our sample, 36 ^{13}CO clumps are gravitationally bound with the virial parameter $\alpha_{\text{vir}} < 2$ and most of them are located in filaments F1 and F2 (see Figure 9). Our results suggest that the bounded cores are mainly formed in the thermally supercritical filaments. In Figure 16, we present the relationship between the mass and virial parameter of the ^{13}CO clump. The fitting line shows a weak anti-correlation between mass and virial parameter ($\alpha_{\text{vir}} \propto M^{-0.21}$), which is similar with the results given by Kauffmann et al. (2013), in the range of $-1 \sim 0$.

Figure 17 depicts the mass-size relation of the clumps. Almost all the clumps are located in the yellow shaded region, which is the area of low-mass star formation according to the

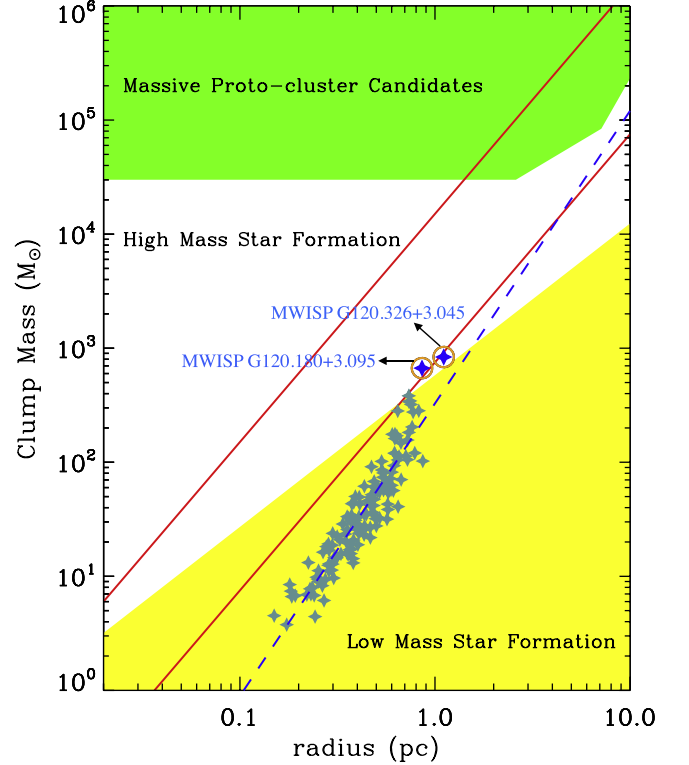


Figure 17. Mass-size relationship of the clumps in the M120.1+3.0 molecular cloud. The yellow shaded region represents the clouds without high-mass star formation, according to the empirical relationship proposed by Kauffmann et al. (2010). The massive proto-clusters are expected in the green shaded region (Bressert et al. 2012). The upper and lower red lines indicate the surface densities of 1 g cm^{-2} (Krumholz & McKee 2008) and 0.05 g cm^{-2} (Urquhart et al. 2013) respectively, which represent the empirical upper and lower bounds of clump surface densities to form massive stars. The cadet blue stars represent the ^{13}CO clumps formed in the M120.1+3.0 cloud. Two blue stars signify the clumps that have potential to form massive stars. The dashed blue line shows the result of a linear least-squares fitting to all the clumps.

empirical relationship in Kauffmann et al. (2010). Nonetheless, it is worth noting that two clumps have surface densities higher than the empirical lower side of surface density for massive star formation (Kauffmann et al. 2010), and one of them has the surface density higher than 0.05 g cm^{-2} (Urquhart et al. 2013). The masses of these two clumps are $836 M_{\odot}$ (MWISP G120.326+3.045) and $668 M_{\odot}$ (MWISP G120.180+3.095), respectively. As affirmed in Figure 7, MWISP G120.326+3.045 is the virialized clump located in the Outflow 1 region, and MWISP G120.180+3.095 is the virialized clump associated with the Outflow 2 region. These two clumps are associated with segments 23, 24 and 25, the regions with the highest accretion rates ($332, 277$ and $261 M_{\odot} \text{ Myr}^{-1}$, as $\alpha = 45^{\circ}$) in the main filament F1. Thus, we suggest that both of the clumps have potential to form massive stars.

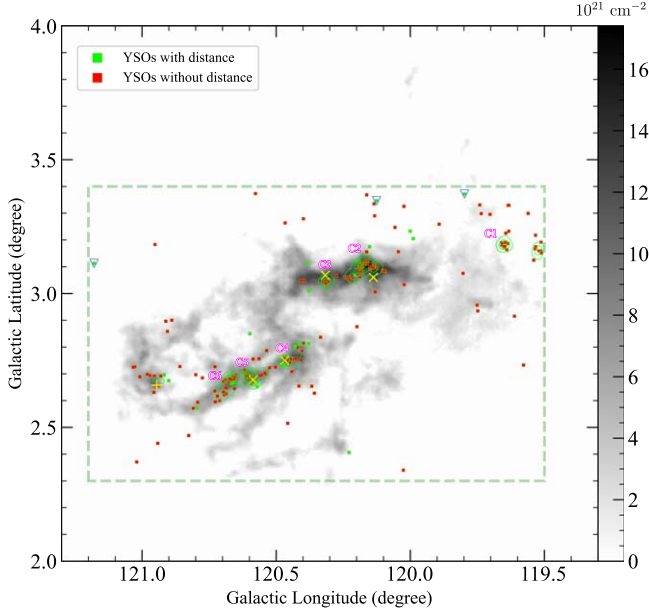


Figure 18. Distribution of identified YSOs on the column density map. The background is the column density calculated from the ^{13}CO emission. The green box shows the selected area for YSO searching. The green and red squares represent the YSO candidates with and without Gaia counterparts, respectively. The green squares enclosed by blue triangles represent the sources outside the 1σ confidence ellipse in the proper motion diagram (see Figure 15). The green contours show the $N=5$ surface density of YSOs. Contour levels are at 4, 8, 12, 20, 28 and 36 stars pc^{-2} . The labels C1-6 represent the clusters (see Section 4.3). The yellow plus (Wouterloot & Brand 1989) and four crosses (Yang et al. 1990) correspond to IRAS sources. From right to left, these five IRAS sources are associated with Outflow 1–5 regions (see Section 4.4), respectively.

4.3. Star Formation Rate

We present the spatial distribution of YSOs on the H_2 column density map in Figure 18. The contours correspond to the surface density of YSO candidates, which is created following the definition of Chavarría et al. (2008). We first make a $6''$ grid and then calculate the surface density of YSOs at each pixel as

$$\Sigma_{\text{YSO}} = \frac{N}{\pi r_N^2}, \quad (15)$$

where r_N is the distance to the $N=5$ nearest neighbor. The contours shown here are smoothed by convolving with a Gaussian kernel of $\text{FWHM} = 10''$. The clear accumulation of abundant YSOs along the main filament F1 forms a YSO chain, which manifests intense star formation activity in the dense part of the filament.

With the obtained YSOs' surface density (Σ_{YSO}), we further create the star formation rate (SFR) surface density (Σ_{SFR}) image, which reflects more precisely how intense the star formation is in the M120.1+3.0 molecular cloud. We assume a

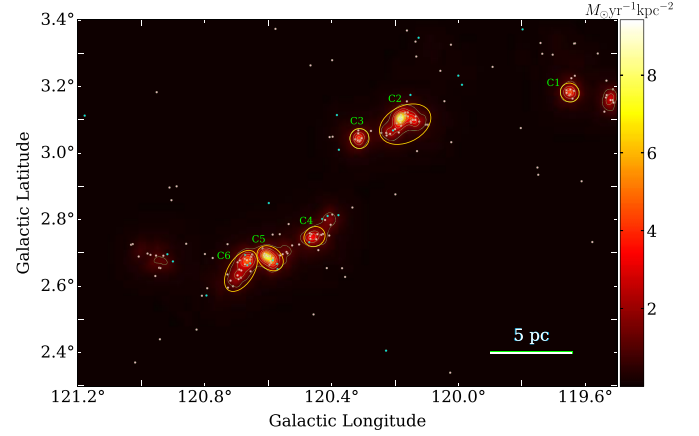


Figure 19. Distribution of SFR surface density. The cyan and pink dots represent the YSO candidates with and without distance, respectively. The contour levels are at 1, 2, 3, 4, 5, 7 and $9 M_{\odot} \text{yr}^{-1} \text{kpc}^{-2}$. The orange ellipses show the clusters identified.

mean mass of $0.5 M_{\odot}$ (Kroupa 2002) and a mean period of 2 Myr (t_{classII}) for star formation (Evans et al. 2009). The Σ_{SFR} is given by $\Sigma_{\text{SFR}} = \frac{\Sigma_{\text{YSO}} \times 0.5}{2}$ in the unit of $M_{\odot} \text{yr}^{-1} \text{kpc}^{-2}$. The distribution of Σ_{SFR} is shown in Figure 19, from which we identify six YSO condensations as clusters (C1–C6). We first choose the sub-regions with peak value of Σ_{SFR} larger than $3 M_{\odot} \text{yr}^{-1} \text{kpc}^{-2}$, and then adjust the areas by visual inspection according to the outer contour of $\Sigma_{\text{SFR}} = 1 M_{\odot} \text{yr}^{-1} \text{kpc}^{-2}$ and the distribution of YSOs. We note that the clusters mostly appear in the high column density regions of the cloud, with one exception C1, which is far away from the M120.1+3.0 cloud. We check the ^{12}CO data cube and consider that cluster C1 is likely associated with another cloud in the velocity range from -40 to -50 km s^{-1} , which is beyond the scope of this work. For clusters C2–C6, we count the number of YSOs in each cluster and compute the mean Σ_{SFR} , as well as the corresponding gas mass surface density (Σ_{gas}). The results are exhibited in Table 3. The clusters have a mean SFR density of $\sim 2 M_{\odot} \text{Myr}^{-1} \text{pc}^{-2}$ on the mean area of $\sim 2.3 \text{ pc}^2$. We plot SFR density as a function of the gas density in Figure 20. As suggested by Zhang et al. (2019), the uncertainties of SFRs are mainly determined by counting statistics. In the process of YSO selection, we need to balance the completeness and purity of the final sample. In this work, we aim to reduce the fraction of fake sources as much as possible, and the cost is that we miss more bona fide YSOs. Moreover, the confusion of extended emission in the star-forming region, combined with the sensitivity of the telescope, will set the flux density limit of identified YSOs, so that the completeness level cannot reach 100%. Also, we only count the YSOs with disks based on the selection criteria. Taking the diskless YSOs into account would increase the total number of YSOs by a factor of 2 (Fang et al. 2012, 2013b). In addition, we assume that all YSOs are singles

Table 3
Properties of Cluster

Name	Glon (deg)	Glat (deg)	Area (pc ²)	Σ_{SFR} ($M_{\odot}\text{Myr}^{-1}\text{pc}^{-2}$)	Σ_{gas} ($M_{\odot}\text{pc}^{-2}$)	$N(\text{YSO})$
C2	120.168	3.087	4.92	1.47	155	7
C3	120.312	3.044	0.95	1.85	148	29
C4	120.454	2.749	1.06	2.13	139	7
C5	120.594	2.684	1.59	2.52	135	16
C6	120.686	2.646	2.95	1.78	119	21

Note. Properties of clusters. Columns 2 and 3 are center coordinates of the clusters identified in Section 4.3. Columns 4–6 are the area, SFR surface density and gas mass surface density of cluster respectively. The last column shows the number of YSOs in different clusters.

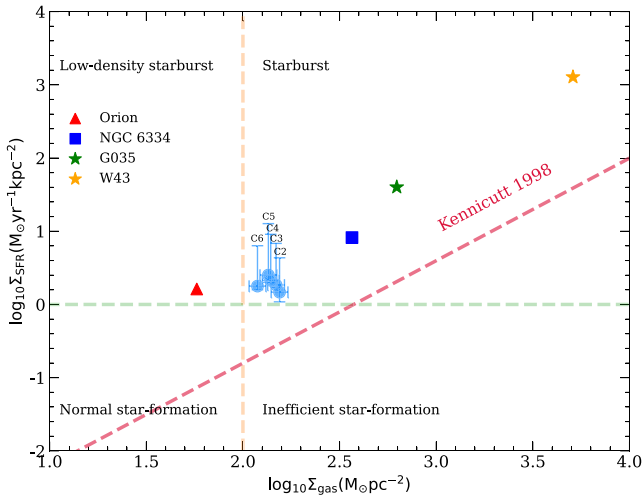


Figure 20. Schmidt–Kennicutt diagram with SFR surface density vs. the gas surface density. The blue dots represent the clusters (C2–6 shown in Figure 19) in the M120.1+3.0 cloud. The horizontal error bar gives a 10% column density error. The vertical error bars represent the upper and lower limits of Σ_{SFR} (see text), respectively. For comparison, we also exhibit other mini-starburst regions in the diagram, such as Orion (Megeath et al. 2012), NGC 6334 (Willis et al. 2013), G035.39–00.33 (Nguyen Luong et al. 2011) and W43 (Motte et al. 2003). The dashed red line represents the Kennicutt–Schmidt relation (Kennicutt 1998).

when calculating SFRs. Actually, more and more studies demonstrate that YSOs are mostly in binary or multiple systems (e.g., Connelley et al. 2008a, 2008b; Chen et al. 2013). Therefore, it is likely that we underestimate the number of YSOs and thus the SFRs. On account of the absence of spectroscopic data and high-resolution data, it is difficult to give an accurate estimate of the SFR uncertainty. Here we simply assume an uncertainty of 50% for SFR. We note that the SFRs of the clusters are slightly larger than $1 M_{\odot} \text{Myr}^{-1} \text{pc}^{-2}$, which is the threshold suggested by Nguyen-Luong et al. (2016) to distinguish mini-starburst from normal star-forming structures. We therefore regard them as mini-starburst cluster candidates. Similar mini-starburst events are also detected in

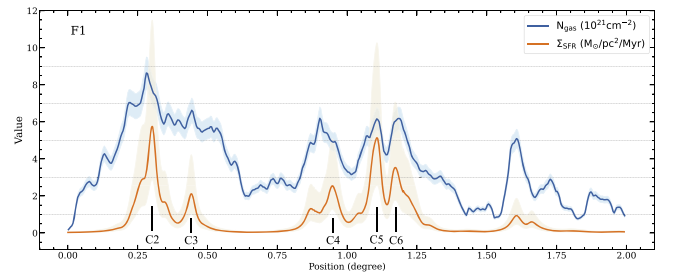


Figure 21. Profiles of SFR surface density Σ_{SFR} and column density N_{gas} along the skeleton of F1. The Σ_{SFR} is derived under the assumption that the mean mass of YSOs is $0.5 M_{\odot}$. The blue and orange shaded areas exhibit the N_{gas} and Σ_{SFR} errors illustrated in Figure 20. The peaks related to clusters are labeled, i.e., C2–6 in Figure 19.

other star-forming regions, such as the active star-forming complexes W43 (Motte et al. 2003) and W48 (Nguyen Luong et al. 2011) and the H II region G154.346+02.606 (Guo et al. 2022).

Lada & Lada (2003) proposed that most stars are born in a clustered configuration, and clusters prefer to form in the overdense regions of molecular clouds (Wu et al. 2005, 2010). To further analyze the relationship between star formation and gas density, we present the comparison between Σ_{SFR} and N_{gas} along the skeleton of F1 in Figure 21. It is of interest to note that the Σ_{SFR} peaks coincide spatially with the gas density enhancements, which confirms the association of YSO candidates to their natal dense gas. Combined with the localized systematic motions appearing in the PV map of F1 (see Figure 7), we suggest that cluster formation is a result of the longitudinal collapse of the filament (Hartmann 2002; Bonnell et al. 2003; Dutta et al. 2018).

4.4. Outflows within Filaments

Observations over a broad range of wavelengths suggest that outflows are ubiquitous in star-forming regions (e.g., Arce et al. 2007; Bally 2016). The rotational transitions of a CO molecule are usually thought to be one of the best tracers for young

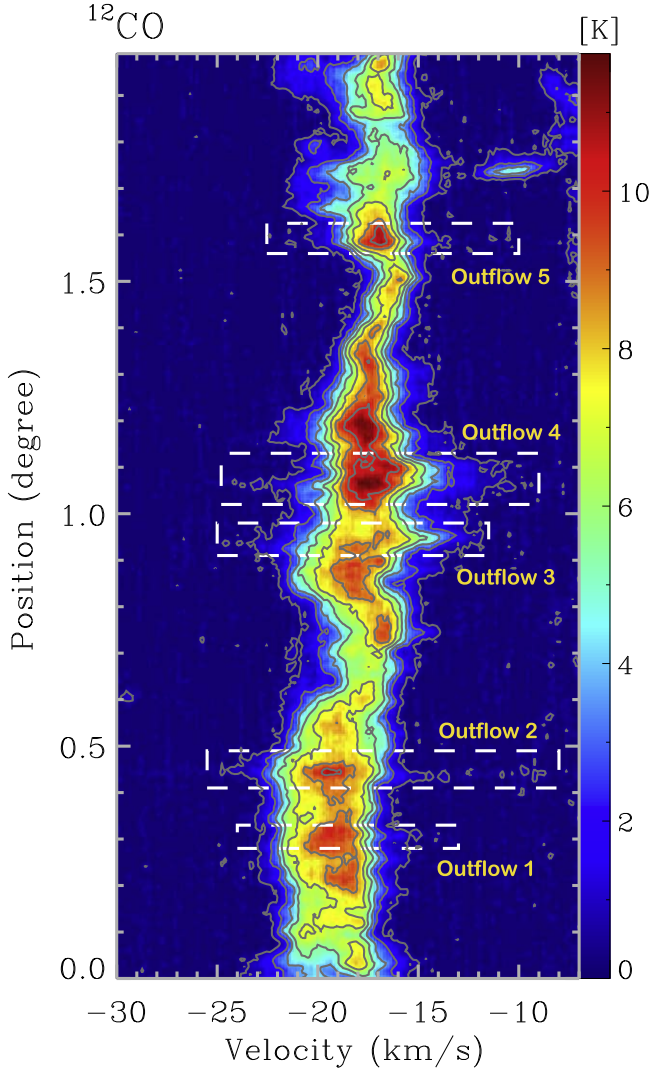


Figure 22. ^{12}CO PV map along the direction of F1 (see Figure 9). The contours start at 3σ with step of 8σ ($\sigma \sim 0.2$ K). The dashed rectangles label the positions of outflow candidates.

outflows (Bally 2016). From the ^{12}CO PV diagram (see Figure 22) along the main filament F1, we find five outflow candidates, which exhibit spur structures. We first check the coordinates of the outflow candidates (see Figure 18) and then extract the feature spectra of ^{12}CO and ^{13}CO at the corresponding positions. The velocities of the ^{13}CO peak emissions are set as the systematic velocities of outflow sources (V_{ISR}). The outflow wings are determined by the ^{12}CO velocity extent, where no clear ^{13}CO emission is detected. Note that the velocity ranges of the outflow wings are also modulated according to the PV diagram. Finally, we integrate the ^{12}CO red- and blue-wing components and superimpose the contours on the ^{12}CO integrated intensity map to check if the wing emission is spatially confined.

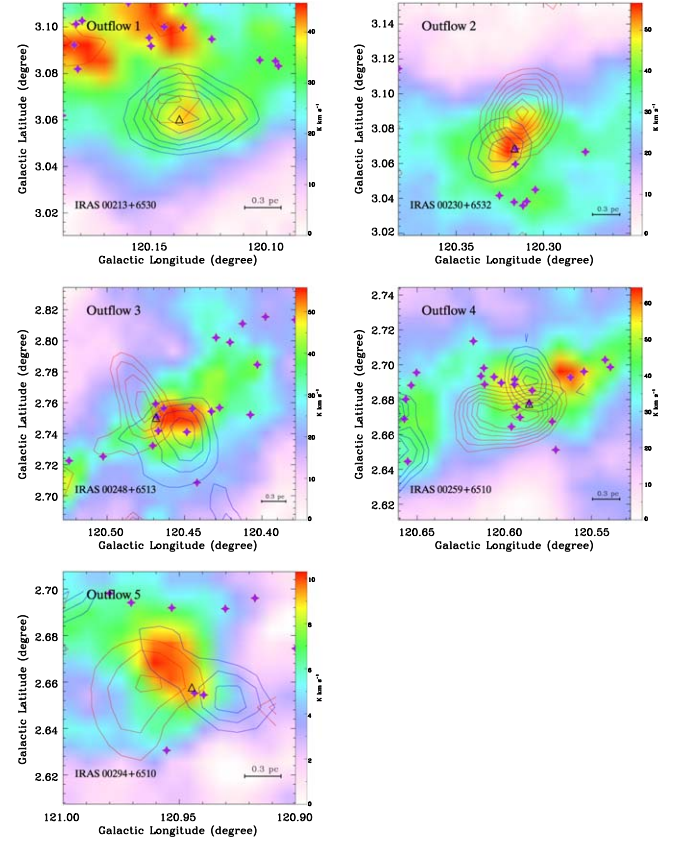


Figure 23. ^{12}CO integrated intensity maps of the outflow regions. The blue and red contours represent the corresponding outflow lobes. The contours start at 3σ with an increment of 1σ ($\sigma \sim 0.6$ K km s $^{-1}$). The black triangles represent the IRAS sources and their names are labeled in the bottom left of each panel. The purple stars signify YSO candidates.

As depicted in Figure 23, all of these five outflows show clear bipolar morphology. The black triangle on each panel represents the IRAS source, which is located nearly in the geometric center of the outflow. The distribution of YSOs identified in Section 3.4 is also exhibited. For Outflows 2, 3 and 4, the central sources IRAS 00230+6532, IRAS 00248+6513 and IRAS 00259+6510 spatially coincide with three YSOs, respectively. For Outflow 5, two YSOs spread near the central source IRAS 00294+6510. Outflows 2, 3 and 5 are newly identified in this work. The relative locations of the sources and lobes favor that IRAS 00230+6532, IRAS 00248+6513 and IRAS 00294+6510 or the YSOs at corresponding locations are the driving sources of Outflows 2, 3 and 5, respectively. Outflows 1 and 4 were studied by Yang et al. (1990) and IRAS 00213+6530 and IRAS 00259+6510 were suggested as their driving sources.

We further calculate the masses of the wing components under the assumption of LTE. We also assume that ^{12}CO gas with high velocity is optically thin. The ^{12}CO column density

Table 4
Properties of Outflows

Outflow	V_{LSR} (km s^{-1})	T_{mb} (K)	V_{red} (km s^{-1})	$N_{\text{H}_2, \text{red}}$ (10^{19} cm^{-2})	M_{red} (M_{\odot})	V_{blue} (km s^{-1})	$N_{\text{H}_2, \text{blue}}$ (10^{19} cm^{-2})	M_{blue} (M_{\odot})	P ($\text{km s}^{-1} M_{\odot}$)	E (10^{44} erg)
Outflow 1	-19.4	7.8	(-16.4, -13.4)	0.90	0.04	(-27.8, -22.8)	1.74	0.12	1.25	0.99
Outflow 2	-19.3	9.3	(-16.0, -10.0)	5.59	0.24	(-29.0, -23.0)	2.36	0.15	3.67	3.46
Outflow 3	-17.5	8.5	(-13.7, -11.5)	2.73	0.22	(-25.0, -21.5)	2.04	0.45	4.70	1.51
Outflow 4	-17.5	10.1	(-14.0, -7.5)	2.71	0.82	(-25.0, -21.0)	1.52	0.23	9.93	9.45
Outflow 5	-17.3	9.1	(-15.0, -10.0)	0.95	0.73	(-23.0, -19.5)	0.72	0.65	9.03	5.97

Note. Properties of outflows. Columns 2 and 3 are the velocity of line center and the main beam temperature respectively. Columns 4–6 are the velocity range, the mean H_2 column density and the mass of the red lobe respectively. Columns 7–9 are the velocity range, the mean H_2 column density and the mass of the blue lobe respectively. Columns 10 and 11 are the total momentum and total energy of outflow respectively.

of an outflow lobe is obtained as follows (Snell et al. 1984)

$$N(^{12}\text{CO}) = 4.2 \times 10^{13} \frac{T_{\text{ex}} \int T_{\text{mb}} dv}{e^{-5.53/T_{\text{ex}}}}, \quad (16)$$

where dv is the velocity range of the red/blue lobe. We adopt the conversion factor $\frac{N(\text{H}_2)}{N(^{12}\text{CO})} \approx 1.1 \times 10^4$ (Frerking et al. 1982) to derive the H_2 column density. The mass of the red/blue lobe is $M_{\text{blue/red}} = \mu m_{\text{H}} \times N_{\text{red/blue}} \times S_{\text{blue/red}}$, where S is the red/blue lobe area. The momentum P and energy E are calculated by $P_{\text{outflow}} = M_{\text{blue}} V_{\text{blue}} + M_{\text{red}} V_{\text{red}}$ and $E_{\text{outflow}} = \frac{1}{2} M_{\text{blue}} V_{\text{blue}}^2 + \frac{1}{2} M_{\text{red}} V_{\text{red}}^2$ respectively, where $V_{\text{blue/red}}$ is the velocity of wing gas relative to the outflow source. The masses, momenta and kinetic energies of outflows are listed in Table 4. Since it is hard to estimate the optical depth effect and the inclination angle, we just give a lower limit of these parameters.

5. Summary

In this paper, we conduct a detailed study toward the M120.1+3.0 molecular cloud, based on the CO molecular line observations from the PMO-13.7 m telescope, IR data from WISE and 2MASS and optical data from Gaia. We investigate the morphology and physical properties of the cloud and analyze the star-forming activities therein. The main results are summarized as follows:

1. The M120.1+3.0 molecular cloud shows filamentary structures in the ^{12}CO and ^{13}CO observations. Combining the DisPerSE algorithm and visual inspection, we identify three filaments, a long S-shaped main filament F1 and two sub-filaments F2 and F3 in the cloud. The main filament F1 also shows clear C^{18}O emission. The basic properties (length, width, excitation temperature, column density, line mass) of each filament have been calculated. Filaments F1 and F2 are thermally supercritical filaments with their LTE line masses higher than the critical line

masses and could be subject to fragmentation. Filament F3 is in a thermally subcritical state.

2. Filament F1 presents clear localized systematic motions in the ^{13}CO PV map, which suggests gas flow converging to the local area caused by longitudinal collapse. We estimate the accretion rates for the segments along F1. The accretion rates range from ~ 35 to $332 M_{\odot} \text{ Myr}^{-1}$ with a mean value of $\sim 132 M_{\odot} \text{ Myr}^{-1}$, under the assumption of inclination angle $\alpha = 45^\circ$.
3. Using the GaussClumps algorithm in the GILDAS package, we identify ~ 150 ^{13}CO clumps, of which 36 are gravitationally bound. Most of the virialized clumps are located in the thermally supercritical filaments F1 and F2. Two clumps with high densities have the potential to form massive stars, according to the mass-size relation. These two clumps are associated with two outflows (Outflow1 and Outflow2), which are located in the filament segments with highest accretion rates.
4. Combined with the IR data from WISE and 2MASS and the optical data from Gaia, we identify ~ 186 YSO candidates. From the distribution of YSOs, we extract five clusters within the dense ridge of F1. Assuming a mean stellar mass of $0.5 M_{\odot}$ and a mean period of 2 Myr, the clusters have a mean SFR surface density of $\Sigma_{\text{SFR}} \sim 2.0 M_{\odot} \text{ Myr}^{-1} \text{ pc}^{-2}$, which indicates that the cloud may be undergoing a mini-starburst event. We further present the profiles of Σ_{SFR} and N_{gas} along the skeleton of F1. The consistency of their distribution indicates that star formation is strongly correlated with dense gas in the molecular cloud.
5. Along the main filament F1, we find five molecular outflows (Outflows 1 ~ 5). Their properties are calculated based on the ^{12}CO data. The emergence of outflows, ^{13}CO virialized clumps and YSOs illustrate that the M120.1+3.0 molecular cloud is undergoing intense star-forming activities.

Acknowledgments

We thank the anonymous referee for providing insightful suggestions and comments, which helped us to improve this work. This work was supported by the National Key R&D Program of China (grant No. 2017YFA0402702), the National Natural Science Foundation of China (NSFC, Grant Nos. 12041305, 12173090 and 12073079) and the CAS International Cooperation Program (grant No. 114332KYSB20190009). We are grateful to all the members of the Milky Way Imaging Scroll Painting (MWISP) CO line survey group, especially the staff of Qinghai Radio Station of PMO at Delingha for the support during the observations. MWISP is sponsored by the National Key R&D Program of China with grant 2017YFA0402701 and the CAS Key Research Program of Frontier Sciences with grant QYZDJ-SSW-SLH047. This research has made use of the NASA/IPAC Infrared Science Archive, which is operated by the Jet Propulsion Laboratory, California Institute of Technology, under contract with the National Aeronautics and Space Administration. This work also has made use of data from the European Space Agency (ESA) mission Gaia (<https://www.cosmos.esa.int/gaia>), processed by the Gaia Data Processing and Analysis Consortium (DPAC, <https://www.cosmos.esa.int/web/gaia/dpac/consortium>). Funding for the DPAC has been provided by national institutions, in particular the institutions participating in the Gaia Multilateral Agreement.

Appendix A

Distance of the M120.1+3.0 Molecular Cloud

In this work, we employ two methods to estimate the distance of the M120.1+3.0 molecular cloud. In the first method, we use a Bayesian approach and model A5 provided by Reid & Dame (2016). The Galactic coordinate and velocity of the source are given to the computer program¹⁰ of Reid & Dame (2016). The program will return different probability density functions (PDFs) and the distance with the greatest integrated probability for the source. We select different positions along the M120.1+3.0 molecular cloud to calculate the mean distance. Ultimately, we derive the distance of 1.1 ± 0.1 kpc for the cloud.

In the second method, we estimate the distance using the extinction method provided by Yan et al. (2019), based on Gaia Data Release 2 (DR2) data. Gaia DR2 permits a more exact measure of the extinction caused by molecular clouds. Thus, a more reliable distance estimate of the cloud can be provided. In theory, stars behind the molecular cloud have higher extinction values A_G . Thus, the extinction value A_G will produce a breakpoint along the l.o.s. because of the existence of the molecular cloud. That is to say, the distance of the cloud can be obtained through the breakpoint in A_G . The result is presented in Figure A1. Considering the 5% systematic parallax error, the

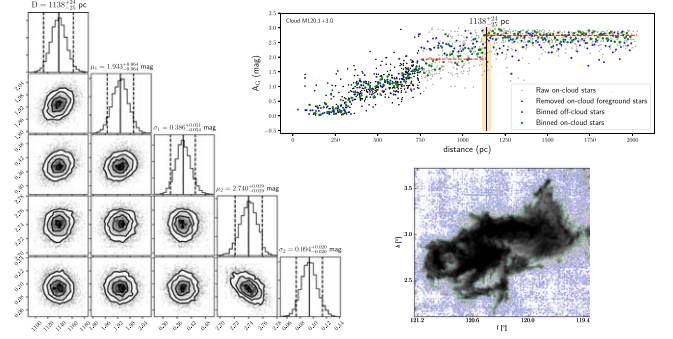


Figure A1. Distance of the M120.1+3.0 molecular cloud. (Bottom right) The ^{12}CO (1-0) integrated intensity image with blue and green contours representing the noise and signal thresholds calculated by Yan et al. (2019) respectively. (Top right) The green and blue points represent on- and off-cloud stars, respectively. The black points correspond to the on-cloud foreground stars. The dashed red lines are the modeled extinction A_G . The distances were derived with raw on-cloud Gaia DR2 stars, which are presented with gray points. The black vertical lines indicate the distance (D) estimated with Bayesian analyses and MCMC sampling, and the shadowed areas depict the 95% highest posterior density (HPD) distance range. The corner plots of the MCMC samples are displayed on the left. The mean and 95% HPD of the samples are shown with solid and dashed vertical lines, respectively, and the systematic uncertainty is not included.

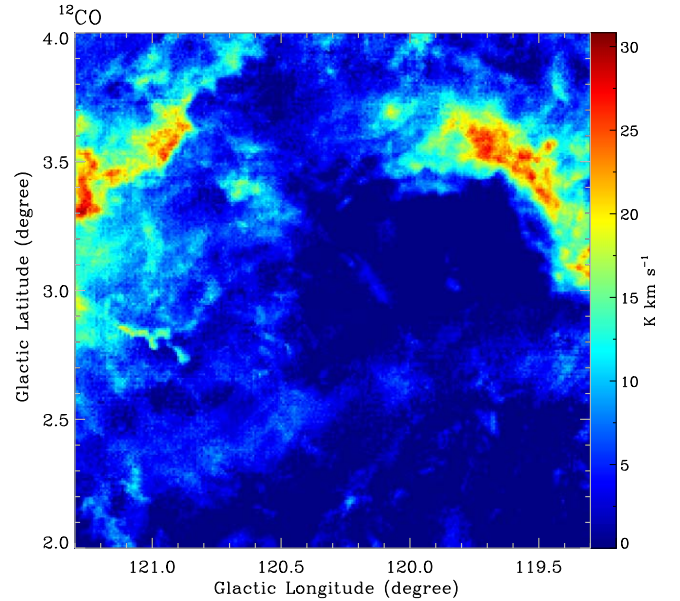


Figure A2. ^{12}CO integrated intensity map of the foreground cloud. The integrated velocity range is between -13.5 and 3.5 km s^{-1} .

distance of this cloud is 1138 ± 58 pc, which is consistent with the result derived from the first method. Thus, we take 1.1 kpc as the distance of the M120.1+3.0 molecular cloud.

Additionally, we also notice a strong foreground extinction phenomenon in Figure A1. The strong foreground component is identified in the velocity range of -13.5 – 3.5 km s^{-1} from Figure 1. We present the ^{12}CO integrated intensity map of the

¹⁰ <http://www.vlbi-astrometry.org/BeSSeL/bayesian>

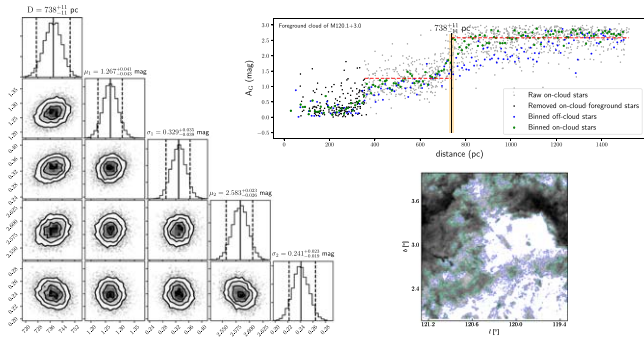


Figure A3. Distance of the foreground cloud. See the caption of Figure A1 for more details.

foreground cloud and measure the distance of the cloud using the extinction method. The results are shown in Figures A2 and A3, respectively. The distance of the foreground cloud is

738 ± 37 pc. According to Equations (1) and (7) the mean excitation temperature and column density of the foreground cloud is 6.76 K and $1.2 \times 10^{21} \text{ cm}^{-2}$, respectively. Adopting the distance of 740 pc, we derive the mass of the foreground cloud with the value of $1.3 \times 10^4 M_{\odot}$ using the CO-to- H_2 mass conversion factor $X = 2.0 \times 10^{20} \text{ cm}^{-2} \text{ K}^{-1} \text{ km}^{-1} \text{ s}$ (Bolatto et al. 2013). The foreground cloud is spatially incomplete in our survey. Wider-field observations are needed to study the distribution and property of the foreground cloud. In this work, we mainly focus on the M120.1+3.0 molecular cloud.

Appendix B

In Table B1, we list the basic properties of the ^{13}CO clumps in the M120.1+3.0 molecular cloud. Also, we present the properties of YSO candidates with and without distance in Tables B2 and B3, respectively.

Table B1
Properties of Clumps in M120.1+3.0 Molecular Cloud

Clump	V_{LSR} (km s^{-1})	T_{ex} (K)	R_{eff} (pc)	$\Delta\nu_{\text{FWHM}}$ (km s^{-1})	c_s (km s^{-1})	σ_{NT} (km s^{-1})	σ_{tot} (km s^{-1})	$n(\text{H}_2)$ (cm^{-3})	M_{LTE} (M_{\odot})	α_{vir}
(1)	(2)	(3)	(4)	(5)	(6)	(7)	(8)	(9)	(10)	(11)
MWISP G120.960+2.667	-17.11	14.80	0.644	1.48	0.208	0.625	0.659	3595	281	1.05
MWISP G120.180+3.095	-19.07	14.17	0.858	2.17	0.203	0.919	0.942	3613	668	1.26
MWISP G120.666+2.692	-17.00	14.88	0.746	1.47	0.208	0.621	0.655	2833	345	0.98
MWISP G120.584+2.680	-17.55	14.79	0.735	1.52	0.208	0.642	0.675	2915	339	1.05
MWISP G120.463+2.747	-17.56	12.72	0.754	1.73	0.193	0.732	0.757	2558	321	1.47
MWISP G120.790+2.587	-17.58	14.43	0.826	1.12	0.205	0.471	0.514	1713	282	0.77
MWISP G120.509+2.866	-16.77	13.32	0.669	1.04	0.197	0.437	0.480	1689	148	1.02
MWISP G120.086+3.081	-18.83	12.80	0.735	2.31	0.193	0.979	0.998	3288	382	2.14
MWISP G120.543+2.785	-16.95	11.13	0.622	1.12	0.180	0.472	0.505	1692	119	1.37
MWISP G120.466+2.665	-17.29	11.86	0.764	1.24	0.186	0.523	0.555	1563	203	1.20
MWISP G120.090+2.669	-18.94	10.56	0.601	0.87	0.175	0.365	0.405	1288	81	1.16
MWISP G120.715+2.642	-18.25	14.14	0.533	1.10	0.203	0.463	0.505	2300	101	1.32
MWISP G120.326+3.045	-18.79	13.04	1.109	2.34	0.195	0.992	1.011	2095	836	1.52
MWISP G120.742+2.740	-16.46	12.78	0.488	0.96	0.193	0.403	0.447	1996	67	1.38
MWISP G120.610+3.021	-17.92	12.27	0.391	1.11	0.189	0.468	0.504	2866	50	2.01
MWISP G120.126+3.022	-19.89	11.51	0.773	1.74	0.183	0.737	0.759	2035	275	1.78
MWISP G120.262+2.426	-19.74	13.10	0.472	1.38	0.195	0.583	0.615	2956	91	2.06
MWISP G120.463+3.147	-20.74	9.57	0.512	1.04	0.167	0.439	0.469	1533	60	1.92
MWISP G120.742+2.401	-16.95	11.15	0.347	0.70	0.180	0.292	0.343	1916	23	1.52
MWISP G121.045+2.740	-15.78	10.37	0.534	1.27	0.174	0.537	0.564	1910	85	2.11
MWISP G120.608+2.500	-17.12	12.64	0.644	0.96	0.192	0.403	0.447	1337	104	1.18
MWISP G119.949+3.050	-17.94	12.64	0.361	0.94	0.192	0.395	0.439	2366	32	2.05
MWISP G120.708+2.770	-16.62	13.49	0.411	0.87	0.198	0.364	0.415	2120	43	1.51
MWISP G121.032+2.833	-17.54	9.69	0.544	1.00	0.168	0.421	0.454	1331	62	1.81
MWISP G120.824+2.881	-17.44	10.17	0.723	1.43	0.172	0.605	0.629	1412	156	1.97
MWISP G120.437+2.996	-17.94	11.54	0.623	1.82	0.183	0.771	0.792	2282	161	2.67
MWISP G120.415+2.802	-19.39	13.65	0.604	1.92	0.199	0.813	0.837	2725	175	2.65
MWISP G120.900+2.749	-17.42	12.31	0.391	0.75	0.189	0.313	0.366	1659	29	1.58
MWISP G121.000+2.775	-15.79	10.88	0.469	1.07	0.178	0.451	0.485	1634	49	2.27
MWISP G120.891+2.588	-16.77	11.87	0.520	0.86	0.186	0.361	0.406	1336	54	1.46
MWISP G121.016+2.644	-16.11	11.28	0.543	1.23	0.181	0.519	0.550	1720	80	2.13
MWISP G120.229+2.825	-19.78	12.00	0.435	1.35	0.187	0.570	0.600	2563	61	2.69
MWISP G120.169+3.157	-19.41	11.90	0.391	0.84	0.186	0.352	0.398	1772	30	1.86
MWISP G120.024+3.049	-19.31	11.29	0.623	2.09	0.181	0.886	0.904	2491	176	3.22
MWISP G120.507+3.039	-18.10	11.13	0.474	1.11	0.180	0.468	0.501	1666	51	2.35
MWISP G120.409+2.758	-16.94	12.19	0.315	0.93	0.189	0.391	0.434	2435	22	2.55
MWISP G120.176+2.951	-19.90	10.75	0.541	1.24	0.177	0.524	0.553	1589	73	2.36
MWISP G120.376+2.661	-18.26	10.32	0.576	0.83	0.173	0.348	0.389	965	54	1.53
MWISP G120.268+2.484	-19.09	12.27	0.457	0.94	0.189	0.395	0.438	1636	45	1.84
MWISP G120.684+2.425	-17.62	11.24	0.436	0.67	0.181	0.279	0.332	1139	27	1.48
MWISP G120.917+2.848	-16.61	10.93	0.564	0.94	0.178	0.395	0.434	1110	58	1.79
MWISP G120.502+2.942	-17.77	10.89	0.620	1.62	0.178	0.686	0.708	1725	120	2.83
MWISP G120.395+3.109	-20.55	12.30	0.735	1.64	0.189	0.694	0.719	1571	182	2.26
MWISP G120.550+2.550	-17.76	12.67	0.600	0.81	0.192	0.339	0.389	993	62	1.31
MWISP G120.591+2.352	-17.94	11.65	0.383	0.94	0.184	0.395	0.436	1811	29	2.37
MWISP G120.649+2.681	-18.76	15.05	0.374	0.91	0.209	0.381	0.435	2242	34	1.89
MWISP G120.016+3.154	-20.26	9.72	0.788	1.11	0.168	0.468	0.498	841	120	1.68
MWISP G120.794+2.801	-16.44	13.02	0.337	1.07	0.195	0.450	0.491	2572	28	2.80
MWISP G120.949+2.759	-16.91	11.20	0.484	0.92	0.181	0.387	0.427	1254	41	2.05
MWISP G120.893+2.650	-16.77	12.61	0.267	0.89	0.192	0.373	0.420	2922	16	2.72
MWISP G121.083+2.542	-16.10	10.10	0.235	0.64	0.172	0.266	0.317	2099	7	2.52
MWISP G120.949+2.565	-16.42	11.78	0.452	1.09	0.185	0.459	0.495	1684	45	2.46
MWISP G120.600+2.965	-18.10	10.84	0.590	1.19	0.178	0.502	0.533	1193	71	2.43
MWISP G120.134+2.648	-20.09	11.06	0.382	0.73	0.180	0.305	0.354	1270	20	2.05
MWISP G120.409+2.715	-16.78	11.34	0.297	1.08	0.182	0.455	0.490	2430	18	3.87
MWISP G120.417+2.843	-18.10	13.23	0.409	1.39	0.196	0.587	0.619	2475	49	3.33
MWISP G119.925+3.018	-18.27	11.05	0.287	1.03	0.179	0.434	0.469	2458	16	3.75

Table B1
(Continued)

Clump	V_{LSR} (km s^{-1})	T_{ex} (K)	R_{eff} (pc)	$\Delta\nu_{\text{FWHM}}$ (km s^{-1})	c_s (km s^{-1})	σ_{NT} (km s^{-1})	σ_{tot} (km s^{-1})	$n(\text{H}_2)$ (cm^{-3})	M_{LTE} (M_{\odot})	α_{vir}
(1)	(2)	(3)	(4)	(5)	(6)	(7)	(8)	(9)	(10)	(11)
MWISP G121.066+2.681	-15.44	11.15	0.253	0.79	0.180	0.331	0.377	2364	11	2.94
MWISP G120.999+2.826	-16.92	10.34	0.574	0.70	0.174	0.292	0.340	695	38	1.53
MWISP G120.792+2.524	-17.10	12.59	0.481	0.77	0.192	0.321	0.374	1118	36	1.64
MWISP G120.226+2.975	-18.45	11.83	0.709	1.22	0.186	0.515	0.547	1084	113	1.95
MWISP G120.191+2.657	-18.93	9.61	0.397	0.96	0.167	0.404	0.438	1410	25	2.96
MWISP G120.448+3.057	-18.43	10.95	0.469	1.12	0.179	0.472	0.505	1385	41	2.94
MWISP G120.434+2.400	-18.59	12.94	0.370	1.06	0.194	0.446	0.486	2061	30	2.84
MWISP G120.734+2.677	-17.27	11.19	0.408	1.06	0.181	0.447	0.482	1677	33	2.87
MWISP G120.109+2.617	-19.26	11.23	0.403	0.62	0.181	0.257	0.314	989	18	1.71
MWISP G120.043+2.918	-19.91	9.68	0.356	0.76	0.168	0.318	0.360	1206	15	2.69
MWISP G120.359+2.757	-18.77	12.10	0.654	1.46	0.188	0.617	0.645	1370	112	2.59
MWISP G120.857+2.709	-17.26	11.51	0.492	0.78	0.183	0.326	0.374	985	34	1.82
MWISP G120.301+2.317	-19.27	11.49	0.373	0.65	0.183	0.270	0.326	1143	17	1.89
MWISP G121.068+2.632	-15.44	12.27	0.402	0.89	0.189	0.373	0.418	1486	28	2.35
MWISP G120.467+2.841	-15.95	11.67	0.247	0.74	0.184	0.309	0.360	2220	9	2.88
MWISP G120.066+2.701	-19.76	11.33	0.413	0.82	0.182	0.344	0.389	1216	25	2.31
MWISP G120.473+3.099	-19.92	11.08	0.545	1.14	0.180	0.481	0.513	1201	56	2.60
MWISP G121.023+2.715	-16.61	10.77	0.371	1.29	0.177	0.545	0.573	2104	31	4.09
MWISP G120.317+2.434	-18.93	12.88	0.485	1.04	0.194	0.437	0.478	1427	47	2.30
MWISP G120.559+2.817	-17.12	11.34	0.370	0.65	0.182	0.270	0.326	1061	15	2.07
MWISP G119.702+2.960	-18.77	10.54	0.299	1.54	0.175	0.652	0.675	3042	23	6.22
MWISP G120.509+2.359	-18.26	11.89	0.385	1.14	0.186	0.481	0.515	1879	31	3.34
MWISP G120.958+2.801	-16.43	9.45	0.354	0.82	0.166	0.344	0.382	1231	16	3.10
MWISP G120.241+3.042	-20.25	11.83	0.355	1.12	0.186	0.472	0.507	1958	25	3.62
MWISP G120.625+2.617	-17.43	13.17	0.330	0.70	0.196	0.291	0.351	1499	15	2.15
MWISP G119.766+2.966	-19.27	9.96	0.617	1.67	0.170	0.707	0.727	1354	93	3.85
MWISP G120.275+2.742	-19.10	10.22	0.436	0.86	0.173	0.361	0.400	1070	25	2.59
MWISP G120.725+2.942	-18.42	10.78	0.284	0.87	0.177	0.365	0.406	1861	12	3.59
MWISP G119.758+3.075	-19.11	10.02	0.595	1.13	0.171	0.477	0.507	928	57	2.78
MWISP G119.833+3.133	-19.11	12.76	0.485	1.15	0.193	0.485	0.522	1408	47	2.85
MWISP G120.675+2.999	-18.10	10.36	0.572	0.89	0.174	0.374	0.412	781	42	2.21
MWISP G120.607+2.732	-17.60	13.11	0.325	1.01	0.195	0.425	0.467	2075	20	3.31
MWISP G120.168+3.123	-21.24	13.30	0.487	1.40	0.197	0.591	0.623	1805	61	3.26
MWISP G120.275+3.110	-22.08	11.12	0.638	2.71	0.180	1.149	1.163	2248	170	5.73
MWISP G121.066+2.860	-16.61	10.32	0.407	0.91	0.173	0.383	0.420	1207	23	2.95
MWISP G120.475+2.575	-17.44	12.92	0.352	0.86	0.194	0.360	0.409	1539	19	2.76
MWISP G120.492+3.016	-18.93	13.66	0.383	1.59	0.200	0.672	0.701	2691	44	4.56
MWISP G120.757+2.974	-17.59	11.09	0.359	0.72	0.180	0.301	0.350	1149	15	2.50
MWISP G120.892+2.824	-17.44	11.96	0.284	1.27	0.187	0.536	0.568	2860	19	4.98
MWISP G119.991+2.909	-19.41	8.08	0.500	0.89	0.153	0.375	0.405	753	27	3.00
MWISP G120.892+2.566	-15.94	11.99	0.229	0.70	0.187	0.291	0.346	2216	7	3.01
MWISP G120.660+2.917	-15.45	10.61	0.286	0.85	0.176	0.357	0.398	1628	11	3.87
MWISP G120.500+3.100	-15.94	11.82	0.240	0.59	0.186	0.244	0.306	1675	6	2.57
MWISP G120.733+2.801	-16.28	11.66	0.192	0.83	0.184	0.348	0.394	3249	6	4.09
MWISP G121.001+2.675	-16.11	11.38	0.180	1.12	0.182	0.472	0.506	4949	8	5.58
MWISP G120.891+2.892	-17.76	12.38	0.445	1.04	0.190	0.438	0.477	1357	35	2.87
MWISP G120.234+3.074	-17.77	12.68	0.182	0.88	0.192	0.369	0.416	4166	7	3.98
MWISP G119.926+3.100	-19.94	9.37	0.612	1.22	0.165	0.516	0.541	840	56	3.37
MWISP G120.992+2.759	-18.26	10.22	0.355	1.74	0.173	0.737	0.757	2554	33	6.72
MWISP G120.842+2.751	-16.77	12.14	0.287	0.86	0.188	0.360	0.407	1862	12	3.44
MWISP G120.568+2.891	-16.77	12.70	0.564	1.37	0.192	0.579	0.610	1279	67	3.29
MWISP G120.850+2.560	-17.09	12.13	0.365	0.74	0.188	0.309	0.361	1196	17	2.45
MWISP G120.041+3.000	-20.25	9.53	0.671	1.21	0.167	0.511	0.538	796	70	2.91
MWISP G119.608+3.032	-20.59	10.44	0.435	1.30	0.174	0.549	0.576	1445	34	4.41
MWISP G120.407+3.058	-17.94	12.41	0.375	1.83	0.190	0.775	0.798	2802	43	6.07
MWISP G120.741+2.725	-18.09	11.03	0.277	1.38	0.179	0.583	0.610	2914	18	6.06
MWISP G120.017+3.099	-20.41	11.92	0.723	1.33	0.186	0.562	0.592	953	105	2.54

Table B1
(Continued)

Clump	V_{LSR} (km s^{-1})	T_{ex} (K)	R_{eff} (pc)	$\Delta\nu_{\text{FWHM}}$ (km s^{-1})	c_s (km s^{-1})	σ_{NT} (km s^{-1})	σ_{tot} (km s^{-1})	$n(\text{H}_2)$ (cm^{-3})	M_{LTE} (M_{\odot})	α_{vir}
(1)	(2)	(3)	(4)	(5)	(6)	(7)	(8)	(9)	(10)	(11)
MWISP G120.409+2.758	-18.27	12.19	0.368	0.76	0.189	0.317	0.369	1168	17	2.60
MWISP G120.918+2.716	-16.77	11.97	0.274	0.68	0.187	0.283	0.339	1553	9	2.83
MWISP G119.717+3.307	-19.75	8.33	0.647	0.84	0.156	0.353	0.386	514	40	2.34
MWISP G120.659+2.492	-17.60	11.89	0.314	0.88	0.186	0.369	0.413	1601	14	3.50
MWISP G119.675+3.108	-19.27	9.31	0.568	0.81	0.165	0.340	0.378	591	31	2.46
MWISP G120.466+2.884	-18.10	12.58	0.502	1.53	0.192	0.647	0.675	1593	59	4.16
MWISP G120.609+2.465	-17.60	11.86	0.220	0.74	0.186	0.309	0.360	2200	6	3.65
MWISP G119.866+2.916	-19.92	9.18	0.866	1.21	0.164	0.511	0.537	537	102	2.59
MWISP G120.774+2.551	-16.77	12.47	0.184	0.87	0.191	0.365	0.411	3612	6	4.40
MWISP G119.975+3.001	-19.75	11.46	0.508	1.55	0.183	0.656	0.681	1438	55	4.62
MWISP G120.268+2.800	-19.60	10.25	0.496	1.00	0.173	0.421	0.455	896	32	3.24
MWISP G119.659+3.176	-19.43	10.74	0.380	0.70	0.177	0.292	0.341	888	14	2.72
MWISP G120.441+2.700	-16.77	12.05	0.174	0.58	0.187	0.239	0.304	2451	3	3.24
MWISP G121.051+2.550	-15.44	10.72	0.270	0.54	0.177	0.223	0.284	1065	6	2.68
MWISP G120.308+2.951	-18.60	11.10	0.433	0.91	0.180	0.382	0.423	972	23	3.24
MWISP G119.925+3.050	-18.43	12.71	0.150	0.80	0.192	0.334	0.386	4582	4	4.44
MWISP G119.759+3.159	-19.60	10.99	0.520	0.90	0.179	0.378	0.418	784	32	2.72
MWISP G119.701+3.042	-19.44	9.62	0.466	1.01	0.167	0.426	0.457	905	26	3.71
MWISP G120.192+3.183	-19.09	12.76	0.250	0.82	0.193	0.343	0.393	2059	9	3.72
MWISP G120.575+3.008	-17.10	10.13	0.467	0.81	0.172	0.340	0.381	734	21	2.93
MWISP G120.533+2.983	-19.09	10.71	0.305	1.11	0.177	0.468	0.500	1764	14	5.37
MWISP G120.309+2.750	-17.27	11.62	0.253	0.83	0.184	0.348	0.393	1903	9	4.04
MWISP G120.758+2.600	-16.60	12.81	0.303	0.62	0.193	0.256	0.321	1188	9	2.52
MWISP G120.976+2.691	-17.94	11.95	0.265	0.69	0.187	0.287	0.342	1525	8	3.18
MWISP G120.534+3.175	-20.92	9.92	0.381	0.70	0.170	0.292	0.338	808	13	2.98
MWISP G121.025+2.600	-15.11	11.70	0.231	0.72	0.185	0.300	0.353	1918	6	3.61
MWISP G120.124+2.974	-19.26	11.66	0.296	0.82	0.184	0.343	0.390	1494	11	3.67
MWISP G120.467+2.692	-17.77	11.68	0.243	0.44	0.185	0.178	0.256	1057	4	2.22
MWISP G120.292+2.975	-17.44	10.79	0.298	0.99	0.177	0.417	0.453	1643	12	4.78
MWISP G120.400+2.700	-17.77	11.28	0.224	1.59	0.181	0.673	0.697	3991	13	8.98

Note. Properties of the identified ^{13}CO clumps. Column 1 is clump name, which is defined according to the Galactic coordinate. Columns 2–4 are the LSR velocity, excitation temperature and effective radius respectively. Columns 5–8 are the linewidth, isothermal sound speed, non-thermal velocity dispersion and total velocity dispersion respectively. Columns 9–11 are the volume density, LTE mass and virial parameter respectively.

Table B2
Basic Information on Identified YSO Candidates (Without Distance)

AllWISE	Glon	Glat	W1(3.4 μm)	W2(4.6 μm)	W3(12 μm)	W4(22 μm)	$J(1.25 \mu\text{m})$	$H(1.65 \mu\text{m})$	$K_s(2.17 \mu\text{m})$	From
(1)	(deg)	(deg)	(mag)	(mag)	(mag)	(mag)	(mag)	(mag)	(mag)	(11)
J002441.85+654908.5	120.195	3.090	12.839	10.473	7.836	2.767	17.12	15.849	14.571	KL14
J002718.76+653032.2	120.433	2.754	12.966	11.711	9.371	6.241	16.174	15.33	14.712	KL14
J002855.11+652642.4	120.593	2.676	14.076	12.017	8.378	4.004				KL14
J002931.45+652718.4	120.657	2.680	10.145	8.75	5.937	3.038	16.626	14.956	13.141	KL14
J002954.81+652659.2	120.696	2.672	14.183	12.259	8.536	4.932				KL14
J002439.65+654727.2	120.188	3.062	12.948	12.009	10.043	7.816	16.915	15.144	13.992	KL14
J002432.14+654950.0	120.179	3.103	11.102	10.136	8.61	6.389	15.466	13.383	12.118	KL14
J002415.55+654859.8	120.150	3.092	12.391	11.448	9.597	8.161	16.327	14.62	13.249	KL14
J002405.69+655000.9	120.135	3.110	12.247	11.411	9.405	7.589	16.179	14.517	13.494	KL14
J002816.33+653302.4	120.535	2.787	12.446	12.177	10.513	8.582	15.716	13.808	12.885	KL14
J002904.81+652808.5	120.612	2.698	12.269	11.025	8.804	6.311	16.704	15.772	14.344	KL14
J002952.88+652539.9	120.691	2.650	12.592	11.633	9.694	7.176	16.749	15.096	13.684	KL14
J002956.83+652439.5	120.697	2.633	12.356	11.59	10.241	8.021	15.733	13.981	12.925	KL14
J001905.20+655348.3	119.633	3.232	12.459	11.688	9.639	7.179	16.452	14.549	13.426	KL14
J002823.03+652747.5	120.539	2.699	12.89	11.495	9.382	4.003	18.738	15.956	14.111	KL14
J001910.32+655107.0	119.636	3.187	12.391	11.393	8.225	6.05	18.277	15.416	14.321	KL14
J002854.29+652620.8	120.591	2.670	11.996	10.811	9.354	6.23	16.75	14.763	13.248	KL14
J001819.15+654640.6	119.540	3.125	12.759	12.141	10.511	8.386	16.205	14.601	13.716	KL14
J002553.06+654638.9	120.312	3.036	12.619	10.632	8.416	4.924	18.663	16.464	15.196	KL14
J002420.07+655009.9	120.160	3.110	12.297	10.175	7.919	4.89	18.242	15.339	13.674	KL14
J002344.17+654808.0	120.095	3.083	12.112	10.912	8.069	5.202	15.349	13.468	12.405	KL14
J002739.14+653031.1	120.468	2.751	8.447	6.541	3.866	1.492	16.296	14.928	11.999	KL14
J002714.13+652428.2	120.415	2.654	11.854	9.856	7.299	4.425	18.394	15.952	14.192	KL14
J002824.52+652803.5	120.542	2.703	11.633	8.526	5.808	2.801	18.733	17.485	15.136	KL14
J002831.87+652743.2	120.554	2.696	8.99	7.619	4.996	2.287	14.862	12.963	10.898	KL14
J002907.48+652905.8	120.618	2.714	12.735	10.614	7.654	4.04	17.452	15.174	14.491	KL14
J002932.58+652510.0	120.655	2.645	11.967	9.156	5.401	2.439				KL14
J002950.58+652719.6	120.690	2.678	10.303	8.415	5.516	2.882	16.469	14.46	12.161	KL14
J003015.03+652459.2	120.729	2.635	15.291	11.542	8.129	4.689				KL14
J003146.64+653910.2	120.905	2.858	12.835	11.015	6.983	3.557	18.508	15.978	14.161	KL14
J003225.89+652545.7	120.956	2.631	11.757	9.935	7.36	4.66	17.0	14.688	12.713	KL14
J002433.15+655021.0	120.182	3.111	11.578	10.624	8.657	5.002	15.564	13.574	12.615	KL14
J002955.48+652357.9	120.693	2.621	10.59	9.482	6.964	4.47	15.72	13.523	12.263	KL14
J003148.50+654128.4	120.911	2.897	11.304	10.504	8.416	6.275	15.902	13.832	12.495	KL14
J003231.98+652938.1	120.971	2.694	12.009	11.086	9.006	5.863	15.906	14.269	13.175	KL14
J002834.05+653122.1	120.563	2.756	10.399	8.55	6.643	3.71	16.412	14.301	12.479	KL14
J002553.55+654837.0	120.316	3.068	13.098	11.216	9.57	4.268	16.726	15.538	14.257	KL14
J002800.59+652911.3	120.503	2.725	14.688	12.542	9.519	4.92				KL14
J003010.46+653025.5	120.728	2.726	13.191	12.045	9.048	4.986	15.975	15.393	14.243	KL14
J002419.03+655253.1	120.163	3.156	11.542	11.216	9.106	7.009	13.446	12.488	12.053	KL14
J002655.33+653359.4	120.398	2.815	12.954	12.385	10.173	8.009	15.318	14.298	13.762	KL14
J002700.07+653210.4	120.403	2.785	10.046	8.383	5.844	3.0	15.939	13.512	11.884	KL14
J002310.06+655208.9	120.044	3.156	11.02	10.437	8.777	6.587	13.299	12.366	11.799	KL14
J002353.31+660044.1	120.133	3.290	12.879	12.4	10.195	7.681	14.674	13.76	13.228	KL14
J002311.63+655740.3	120.057	3.247	12.36	11.648	9.592	7.374	15.13	13.945	13.024	KL14
J002847.08+653125.1	120.586	2.755	11.893	11.481	9.962	8.372	13.998	13.067	12.593	KL14
J002836.46+652733.8	120.562	2.693	11.803	11.045	8.915	4.53	15.205	13.725	12.778	KL14
J002849.50+652713.8	120.584	2.685	9.721	8.969	6.844	4.268	12.649	11.456	10.694	KL14
J002941.52+652730.9	120.674	2.682	10.447	9.411	7.722	5.761	15.093	13.124	11.829	KL14
J002941.83+652631.9	120.673	2.666	12.83	11.603	8.932	5.542	15.652	14.487	13.711	KL14
J002745.51+651622.7	120.457	2.515	11.593	10.972	8.626	7.082	13.108	12.604	12.234	KL14
J003039.35+652809.9	120.775	2.685	8.006	7.437	4.887	2.8	10.234	9.565	8.934	KL14
J003052.94+652859.7	120.799	2.697	10.28	9.939	7.693	5.376	12.02	11.256	10.806	KL14
J003135.28+654135.2	120.889	2.900	9.186	8.386	6.445	4.275	13.045	11.324	10.241	KL14
J003125.61+653106.8	120.859	2.727	11.973	11.28	9.353	7.353	13.863	12.873	12.383	KL14
J003217.97+652711.2	120.944	2.655	8.288	7.228	5.086	2.368	13.481	11.486	10.014	KL14
J001758.37+655028.0	119.513	3.192	6.542	5.439	2.836	0.602	12.469	10.259	8.549	KL14

Table B2
(Continued)

AllWISE	Glon	Glat	W1(3.4 μm)	W2(4.6 μm)	W3(12 μm)	W4(22 μm)	$J(1.25 \mu\text{m})$	$H(1.65 \mu\text{m})$	$K_s(2.17 \mu\text{m})$	From
(1)	(deg)	(deg)	(mag)	(mag)	(mag)	(mag)	(mag)	(mag)	(mag)	(11)
	(2)	(3)	(4)	(5)	(6)	(7)	(8)	(9)	(10)	
J002555.90+654648.1	120.317	3.038	13.824	13.051	12.169	7.252	17.519	16.075	14.372	KW12
J002548.43+654709.0	120.305	3.045	13.054	11.833	12.554	9.021	17.683	16.133	14.597	KW12
J002600.61+654704.4	120.325	3.042	10.458	10.032	10.064	9.251	16.078	12.807	11.203	KW12
J002554.24+654805.6	120.316	3.060	13.53	12.56	11.667	8.668	17.712	15.246	13.943	KW12
J002530.43+654816.5	120.276	3.067	14.019	13.263	12.686	9.158	17.37	16.145	14.87	KW12
J002511.88+654743.5	120.243	3.061	13.12	12.503	12.308	9.032	18.452	15.08	13.631	KW12
J002502.55+654709.7	120.227	3.053	14.237	13.256	12.183	9.196	18.417	16.538	14.692	KW12
J002502.77+654738.0	120.228	3.061	13.863	13.141	12.211	9.142	17.549	15.791	14.369	KW12
J002455.83+654722.6	120.216	3.058	13.595	12.989	12.029	9.167	17.64	15.574	14.215	KW12
J002641.77+654756.9	120.397	3.049	13.884	13.247	12.645	9.151	18.676	15.639	14.473	KW12
J002647.36+654756.4	120.406	3.048	12.604	11.944	12.581	9.041	17.037	14.559	13.108	KW12
J002445.86+654808.2	120.200	3.072	13.722	13.182	11.532	9.136	17.844	15.961	14.475	KW12
J002434.47+654836.3	120.181	3.082	13.353	12.798	11.106	9.219	18.106	15.576	13.93	KW12
J002438.51+654948.2	120.190	3.101	12.974	11.567	12.259	9.125	17.368	16.149	14.181	KW12
J002437.32+655000.3	120.189	3.105	13.921	12.609	12.175	9.144	18.298	17.433	15.027	KW12
J002424.54+655021.4	120.167	3.113	12.074	9.876	6.921	3.776	18.321	15.894	13.789	KW12
J002415.77+654912.9	120.151	3.095	14.246	13.319	11.863	8.246	14.868	14.068	14.566	KW12
J002424.78+655052.6	120.169	3.121	14.065	13.428	11.432	9.296	17.579	16.123	14.548	KW12
J002411.69+654927.2	120.144	3.100	14.455	13.665	12.411	8.593	17.793	16.442	15.142	KW12
J002419.59+655052.3	120.160	3.122	12.951	12.412	11.415	9.105	18.207	14.92	13.551	KW12
J002407.07+654923.0	120.136	3.100	14.203	13.407	12.05	9.036	18.348	16.523	14.988	KW12
J002400.15+654900.5	120.124	3.095	14.191	13.421	12.355	8.834	18.61	16.836	15.134	KW12
J002348.69+654820.3	120.103	3.086	14.047	13.216	12.134	8.882	18.659	15.679	14.838	KW12
J002344.79+654816.3	120.096	3.085	14.028	13.075	11.501	8.464	18.589	17.408	14.974	KW12
J002715.61+653039.2	120.427	2.757	13.334	12.832	12.184	8.239	17.529	15.437	14.039	KW12
J002739.26+653101.9	120.469	2.759	11.984	11.46	10.835	7.272	16.428	13.762	12.564	KW12
J002813.38+652908.5	120.525	2.723	13.211	11.93	8.794	5.724	18.66	16.084	15.125	KW12
J002855.19+652729.2	120.594	2.689	12.883	12.21	12.194	9.061	18.017	15.316	13.634	KW12
J002905.98+652752.5	120.613	2.693	13.097	11.525	8.796	5.638	17.542	16.486	14.807	KW12
J002905.03+652734.9	120.611	2.689	13.299	12.747	10.455	6.008	16.308	14.933	13.909	KW12
J002857.38+652602.9	120.596	2.664	13.139	11.4	9.386	6.151	18.482	16.797	14.666	KW12
J002927.15+652811.2	120.650	2.695	13.384	12.403	11.407	5.57	18.842	16.581	14.239	KW12
J002929.28+652746.0	120.653	2.688	10.891	8.333	4.82	1.376	18.184	15.61	13.772	KW12
J002937.50+652714.7	120.667	2.678	6.064	5.185	5.13	4.611	13.767	9.225	6.888	KW12
J002951.04+652411.4	120.686	2.626	12.142	11.495	12.346	9.181	16.88	14.102	12.624	KW12
J003006.62+652246.4	120.711	2.600	14.551	13.894	12.411	9.071	18.455	16.687	15.009	KW12
J003015.93+652235.5	120.727	2.595	14.211	13.499	12.593	9.064	18.058	16.629	14.715	KW12
J003053.56+652248.9	120.792	2.594	13.352	12.609	12.282	9.052	17.706	15.504	13.812	KW12
J003104.16+652132.2	120.809	2.571	14.032	12.767	12.595	9.122	18.242	15.925	14.911	KW12
J001941.29+655805.9	119.703	3.296	14.531	13.931	10.349	7.008	16.918	15.682	15.033	KW12
J003159.30+655848.4	120.952	3.183	13.316	12.534	10.322	7.915	16.793	16.097	14.847	KW12
J003237.19+652954.6	120.981	2.698	9.998	9.487	9.625	8.987	15.033	12.05	10.602	KW12
J001909.90+652338.8	119.578	2.733	13.511	12.184	9.646	7.624	17.016	16.109	15.11	KW12
J003302.90+653148.8	121.027	2.727	14.084	13.495	12.711	9.132	18.674	15.968	14.732	KW12
J003306.05+653143.4	121.032	2.725	11.658	10.966	11.5	9.194	17.675	14.307	12.366	KW12
J003313.15+651029.0	121.020	2.371	14.181	13.413	10.841	8.751	16.802	15.993	15.112	KW12
J002725.81+653042.8	120.445	2.756	9.684	9.189	8.04	4.694	12.117	10.878	10.626	KW12
J003208.73+652917.8	120.931	2.692	14.292	13.634	12.762	9.248	16.276	15.252	14.79	KW12
J002350.67+650321.2	120.026	2.340	13.6	12.813	10.338	8.221	17.402	17.217	14.883	KW12
J002134.57+655716.1	119.892	3.259	13.469	12.953	10.356	7.606	15.419	14.558	14.219	KW12
J001801.24+654831.6	119.513	3.159	10.222	9.493	6.915	4.395	13.68	12.182	11.555	KW12
J002551.65+654646.7	120.310	3.038	12.96	11.763	9.189	5.618	17.067	15.646	14.281	HKW
J002434.74+654913.9	120.183	3.092	11.027	10.224	6.591	4.079	15.902	13.375	12.2	HKW
J002433.74+654945.8	120.182	3.101	13.474	12.77	11.655	6.259	16.571	14.76	14.042	HKW
J002432.58+655030.6	120.181	3.114	12.07	10.569	8.252	4.401	16.691	15.946	13.818	HKW
J002409.70+654345.5	120.131	3.006	13.287	12.984	11.991	9.123	16.342	14.791	14.072	HKW
J002709.43+653308.3	120.421	2.799	13.986	13.361	12.627	9.083	16.206	15.357	14.834	HKW

Table B2
(Continued)

AllWISE	Glon	Glat	W1(3.4 μm)	W2(4.6 μm)	W3(12 μm)	W4(22 μm)	$J(1.25 \mu\text{m})$	$H(1.65 \mu\text{m})$	$K_s(2.17 \mu\text{m})$	From
(1)	(deg)	(deg)	(mag)	(mag)	(mag)	(mag)	(mag)	(mag)	(mag)	(11)
	(2)	(3)	(4)	(5)	(6)	(7)	(8)	(9)	(10)	
J002704.42+653016.1	120.407	2.752	13.83	13.09	12.253	6.43	17.259	15.879	14.882	HKW
J002305.42+654439.8	120.023	3.033	14.029	13.604	11.185	8.399	16.608	15.62	14.883	HKW
J002736.37+653050.2	120.463	2.756	13.434	12.558	10.342	5.168	18.377	15.297	14.074	HKW
J002629.64+660141.8	120.398	3.279	12.732	12.601	11.831	8.747	16.317	15.115	14.205	HKW
J002739.19+652958.8	120.467	2.742	14.33	13.058	10.329	6.75	15.905	14.986	14.917	HKW
J002710.53+660109.1	120.467	3.264	14.062	13.785	11.712	9.051	16.928	15.574	14.944	HKW
J002726.61+652750.7	120.442	2.708	11.592	11.511	11.677	8.754	14.521	14.333	13.899	HKW
J002351.94+660325.3	120.135	3.335	13.399	13.108	9.859	8.181	16.804	15.447	14.501	HKW
J002854.91+652739.7	120.594	2.692	13.912	13.598	11.952	9.048	17.208	15.318	14.675	HKW
J002246.96+660208.2	120.024	3.326	13.11	12.942	12.018	8.921	15.713	15.089	14.356	HKW
J002809.58+660819.0	120.577	3.373	12.714	12.541	10.636	8.969	15.176	14.437	14.322	HKW
J002055.42+654541.6	119.803	3.075	13.269	12.608	12.317	8.983	15.168	14.344	14.166	HKW
J003010.30+652349.3	120.719	2.617	13.386	12.71	10.551	8.909	15.88	14.773	14.021	HKW
J002000.32+655830.2	119.736	3.299	14.341	13.16	8.106	6.94	16.264	15.356	15.028	HKW
J002001.22+660028.6	119.741	3.331	14.458	13.336	7.631	7.218	16.326	15.299	15.289	HKW
J001924.21+655056.8	119.659	3.181	13.509	13.003	9.3	8.817	16.659	15.868	14.936	HKW
J001923.77+655126.6	119.659	3.189	13.325	12.895	7.967	6.292	16.872	15.639	14.917	HKW
J001919.73+655026.5	119.650	3.174	13.689	13.175	7.727	6.576	16.903	15.875	15.224	HKW
J001917.69+655035.1	119.647	3.177	12.679	12.078	6.659	5.014	16.108	14.981	14.147	HKW
J001914.51+654946.9	119.640	3.164	14.135	13.406	12.592	8.364	16.822	15.505	14.684	HKW
J001916.27+655127.6	119.647	3.191	11.289	10.516	7.494	5.44	15.932	14.449	13.545	HKW
J001912.13+655327.4	119.644	3.225	13.391	12.329	9.559	5.865	16.87	15.572	14.568	HKW
J003222.00+652925.4	120.954	2.692	12.763	12.564	9.978	8.041	16.431	14.987	14.151	HKW
J001859.49+655935.2	119.635	3.329	14.257	13.698	11.26	7.623	15.925	15.532	15.119	HKW
J001857.69+655936.1	119.632	3.330	13.618	13.507	11.728	8.394	16.085	15.409	15.015	HKW
J003118.42+651532.1	120.826	2.470	12.002	11.94	11.278	8.564	14.872	13.748	13.082	HKW
J003253.59+652929.6	121.008	2.689	13.924	13.752	12.7	8.771	17.148	15.468	14.896	HKW
J001811.15+654935.2	119.532	3.174	11.661	11.179	5.473	3.845	13.496	12.972	12.682	HKW
J001805.26+654835.9	119.520	3.159	11.933	11.513	7.047	4.954	16.564	15.446	13.94	HKW
J003225.64+651419.5	120.941	2.441	13.567	13.209	11.898	8.9	16.372	15.655	14.877	HKW
J002457.10+653625.6	120.199	2.876	13.303	13.099	11.922	8.69	16.651	15.461	14.615	HKW
J002617.65+653452.8	120.334	2.836	13.336	12.589	10.164	8.095	15.877	14.772	14.034	HKW
J002728.63+652950.2	120.448	2.741	12.711	11.814	9.553	6.696	15.735	14.381	13.585	HKW
J002646.58+652410.5	120.367	2.654	13.993	13.615	12.555	8.883	16.666	15.531	14.897	HKW
J002642.54+652233.0	120.357	2.628	12.119	11.287	6.9	4.858	15.864	14.718	13.908	HKW
J002405.70+660535.2	120.162	3.369	13.18	12.46	7.266	4.127	16.61	15.547	15.17	HKW
J002859.47+652735.1	120.602	2.690	11.822	11.058	8.891	5.879	14.599	13.425	12.783	HKW
J002901.68+652748.5	120.606	2.693	8.218	7.318	5.587	3.823	11.889	10.441	9.508	HKW
J002949.31+652528.5	120.685	2.647	10.408	9.645	7.782	5.538	14.528	12.593	11.483	HKW
J003215.70+652707.2	120.940	2.654	8.831	7.908	5.222	2.527	11.166	10.463	9.93	HKW
J002033.32+653814.9	119.751	2.957	13.989	13.407	8.082	6.205	16.654	15.776	15.4	HKW
J002033.40+653656.0	119.748	2.935	11.913	10.886	7.988	6.408	16.809	15.089	13.748	HKW
J001916.01+653446.4	119.612	2.915	13.628	13.163	11.855	9.068	16.358	15.238	14.53	HKW
J001813.00+654909.7	119.535	3.167	12.037	11.745	6.689	4.991	15.558	14.41	14.041	HKW
J001808.32+655210.7	119.533	3.218	13.052	13.021	7.49	5.407	16.36	15.12	14.539	HKW
J001818.07+655714.4	119.561	3.299	14.16	13.632	11.362	8.567	16.857	15.691	14.984	HKW
J001800.69+654809.8	119.512	3.153	11.448	11.124	7.203	5.102	14.589	13.153	12.45	HKW
J001800.30+654802.6	119.511	3.151	12.003	11.384	6.825	4.388	16.204	14.64	13.889	HKW

Note. Basic information on the identified YSO candidates. Column 1 lists the YSO ID from the AllWISE catalog. Columns 2 and 3 are their Galactic coordinates. Columns 4–7 show the photometric magnitudes of the WISE W1, W2, W3 and W4 bands respectively. Columns 8–10 express the photometric magnitudes of the 2MASS J , H and K_s bands respectively. Column 11 provides the selection system from which IR-excess sources are identified.

Table B3
Basic Information on Identified YSO Candidates (with distance)

AllWISE (1)	Glon (deg) (2)	Glat (deg) (3)	W1 (3.4 μ m) (mag) (4)	W2 (4.6 μ m) (mag) (5)	W3 (12 μ m) (mag) (6)	W4 (22 μ m) (mag) (7)	J (1.25 μ m) (mag) (8)	H (1.65 μ m) (mag) (9)	K _s (2.17 μ m) (mag) (10)	From (11)	Gaia EDR3 (12)	Plx (arcsec) (13)	pmRA (mas yr ⁻¹) (14)	pmDE (mas yr ⁻¹) (15)	G (mag) (16)	G – RP (mag) (17)
J002239.49 +655626.2	120.000	3.233	11.519	11.017	8.641	6.502	14.117	13.094	12.523	KL14	Gaia EDR3 527,447,826,771,619,328 ^c	0.8253	-2.388	-0.901	17.025	1.156
J002632.47 +654529.3	120.377	3.010	12.465	11.965	10.146	7.901	14.94	13.848	13.193	KL14	Gaia EDR3 527,450,025,796,384,896 ^c	0.8291	-2.439	-0.727	18.613	1.306
J002849.19 +653708.9	120.598	2.850	11.665	11.354	9.752	8.067	13.789	12.747	12.194	KL14	Gaia EDR3 527,397,695,913,877,888 ^c	0.8601	-2.495	0.188	17.086	1.230
J003152.04 +652808.1	120.900	2.674	12.641	12.167	9.69	7.222	14.952	13.816	13.336	KL14	Gaia EDR3 527,381,130,220,679,936 ^c	0.8668	-1.82	-1.075	18.116	1.190
J002843.45 +652507.3	120.570	2.651	9.136	8.566	6.13	4.102	11.519	10.643	10.0	KL14	Gaia EDR3 527,371,067,116,703,104 ^c	0.8695	-1.961	-0.727	14.273	1.017
J002843.82 +652606.1	120.573	2.667	10.683	10.026	7.72	5.461	13.801	12.492	11.703	KL14	Gaia EDR3 527,371,097,178,865,792 ^c	0.8718	-2.003	-1.215	18.059	1.340
J002644.38 +653346.1	120.379	2.814	11.78	11.15	9.135	7.336	15.093	13.782	13.054	KL14	Gaia EDR3 527,422,950,321,406,464 ^c	0.8799	-1.733	-0.394	17.830	1.291
J002449.85 +654757.1	120.206	3.068	12.916	12.494	10.087	7.886	15.314	14.07	13.519	KL14	Gaia EDR3 527,430,539,525,020,928 ^c	0.8886	-2.839	-1.468	19.414	1.536
J002850.81 +652648.8	120.586	2.678	8.757	7.819	5.724	3.064	11.43	10.121	9.251	KL14	Gaia EDR3 527,371,513,793,294,848 ^c	0.9076	-1.803	-0.754	17.099	1.575
J002704.12 +653348.5	120.413	2.811	9.055	8.377	6.457	4.262	11.748	10.665	9.919	KL14	Gaia EDR3 527,423,087,760,362,240 ^c	0.913	-1.852	-0.288	14.746	1.072
J003201.19 +652930.7	120.918	2.696	12.21	11.754	9.467	7.285	15.019	13.676	12.944	KL14	Gaia EDR3 527,381,198,940,178,560 ^c	0.9194	-1.923	-0.681	17.756	1.259
J002630.20 +655145.8	120.383	3.114	12.07	11.322	8.931	6.687	14.952	13.801	12.961	KL14	Gaia EDR3 527,452,289,239,461,248 ^c	0.941	-2.254	-0.653	18.676	1.210
J002937.69 +652621.7	120.666	2.664	11.504	10.663	8.241	5.956	14.434	13.287	12.532	KL14	Gaia EDR3 527,371,994,829,640,832 ^c	0.9478	-2.224	-0.599	17.784	1.338
J003055.93 +652131.0	120.795	2.572	10.915	10.223	8.278	6.21	13.58	12.431	11.816	KL14	Gaia EDR3 527,358,938,129,105,024 ^c	0.9498	-1.865	-0.761	17.209	1.294
J002741.75 +652925.7	120.470	2.732	11.273	10.727	8.736	5.959	13.539	12.897	12.044	KL14	Gaia EDR3 527,375,396,439,434,112 ^c	1.0346	-2.007	-1.402	19.973	1.619
J002031.43 +660319.4	119.798	3.372	12.89	12.416	12.335	9.29	13.648	13.201	12.963	KL14	Gaia EDR3 528,201,645,072,228,864	1.0402	6.808	1.865	15.766	0.906
J002411.31 +655357.7	120.151	3.175	12.157	11.457	9.548	7.488	15.193	14.029	13.314	KL14	Gaia EDR3 527,443,355,707,571,456 ^c	1.0403	-2.295	-1.392	19.188	1.400
J002714.47 +653322.0	120.430	2.802	10.701	9.789	7.402	5.071	14.499	13.001	12.059	KL14	Gaia EDR3 527,376,148,058,873,472 ^c	1.0413	-1.898	-0.768	18.732	1.418
J002541.34 +650833.6	120.228	2.406	13.99	13.195	8.751	6.239	16.62	15.434	14.581	HKW	Gaia EDR3 527,311,689,191,274,752 ^c	0.8149	-2.253	-0.171	20.045	1.123
J003415.48 +655533.4	121.179	3.113	13.439	12.911	11.792	8.967	15.617	14.955	14.646	HKW	Gaia EDR3 527,587,597,891,492,992	0.8161	-0.703	0.789	19.765	1.162
J002234.52 +655443.2	119.989	3.205	14.256	13.635	10.937	8.772	16.181	15.337	15.114	HKW	Gaia EDR3 527,446,207,567,286,912 ^c	0.8268	-2.434	-1.027	20.164	1.470
J002345.43 +660403.2	120.126	3.347	14.035	13.456	9.217	6.852	16.91	15.856	15.0	HKW	Gaia EDR3 527,470,121,945,220,608	0.8341	-3.876	0.091	20.812	1.153
J002932.47 +652637.7	120.657	2.669	9.729	9.074	7.277	5.824	12.244	11.335	10.777	HKW	Gaia EDR3 527,371,994,829,637,760 ^c	0.8672	-2.226	-0.572	15.246	1.137
J002940.09 +652811.1	120.673	2.694	12.003	10.733	8.112	4.705	15.869	14.813	13.874	HKW	Gaia EDR3 527,372,505,928,231,808 ^c	0.9896	-2.368	-1.148	19.686	1.346

Note. Basic information on the identified YSO candidates. The captions of Columns 1–11 are the same as those in Table B2. Column 12 lists the Gaia EDR3 ID. The EDR3 ID with the label “c” is the co-moving member identified in Section 3.4. Columns 13–15 express the parallax, and proper motions in R.A. and decl. directions respectively. Columns 16 and 17 show the photometric magnitudes in G band and the magnitude differences between G and RP bands respectively.

ORCID iDs

Li Sun, <https://orcid.org/0000-0003-2732-0592>
 Xuepeng Chen, <https://orcid.org/0000-0003-3151-8964>
 Min Fang, <https://orcid.org/0000-0001-8060>
 Weihua Guo, <https://orcid.org/0000-0002-8589-9611>
 Yan Sun, <https://orcid.org/0000-0002-3904-1622>
 Yang Su, <https://orcid.org/0000-0002-0197-470X>
 Shaobo Zhang <https://orcid.org/0000-0003-2549-7247>
 Miaomiao Zhang <https://orcid.org/0000-0002-6388-649X>
 Xiao-Long Wang <https://orcid.org/0000-0003-2536-3142>
 Xin Zhou <https://orcid.org/0000-0003-2418-3350>
 Ji Yang, <https://orcid.org/0000-0001-7768-7320>

References

- Allen, L., Megeath, S. T., Gutermuth, R., et al. 2007, in *Protostars and Planets V*, ed. B. Reipurth, D. Jewitt, & K. Keil (Tucson, AZ: Univ. Arizona Press), 361
- André, P., Men'shchikov, A., Bontemps, S., et al. 2010, *A&A*, 518, L102
- Arce, H. G., Shepherd, D., Gueth, F., et al. 2007, in *Protostars and Planets V*, ed. B. Reipurth, D. Jewitt, & K. Keil (Tucson, AZ: Univ. Arizona Press), 245
- Arzoumanian, D., André, P., Didelon, P., et al. 2011, *A&A*, 529, L6
- Arzoumanian, D., André, P., Peretto, N., & Könyves, V. 2013, *A&A*, 553, A119
- Bally, J. 2016, *ARA&A*, 54, 491
- Bessell, M. S., & Brett, J. M. 1988, *PASP*, 100, 1134
- Beuther, H., Ragan, S. E., Johnston, K., et al. 2015, *A&A*, 584, A67
- Bolatto, A. D., Wolfire, M., & Leroy, A. K. 2013, *ARA&A*, 51, 207
- Bonnell, I. A., Bate, M. R., & Vine, S. G. 2003, *MNRAS*, 343, 413
- Bonnor, W. B. 1956, *MNRAS*, 116, 351
- Bourke, T. L., Garay, G., Lehtinen, K. K., et al. 1997, *ApJ*, 476, 781
- Bressert, E., Ginsburg, A., Bally, J., et al. 2012, *ApJL*, 758, L28
- Burkert, A., & Hartmann, L. 2004, *ApJ*, 616, 288
- Chavarría, L. A., Allen, L. E., Hora, J. L., Brunt, C. M., & Fazio, G. G. 2008, *ApJ*, 682, 445
- Chen, X., Arce, H. G., Zhang, Q., et al. 2013, *ApJ*, 768, 110
- Clarke, S. D., Whitworth, A. P., Duarte-Cabral, A., & Hubber, D. A. 2017, *MNRAS*, 468, 2489
- Connelley, M. S., Reipurth, B., & Tokunaga, A. T. 2008a, *AJ*, 135, 2496
- Connelley, M. S., Reipurth, B., & Tokunaga, A. T. 2008b, *AJ*, 135, 2526
- Cutri, R. M., Wright, E. L., Conrow, T., et al. 2013, Explanatory Supplement to the ALLWISE Data Release Products, <http://wise2.ipac.caltech.edu/docs/release/allwise/expsup>
- Dutta, S., Mondal, S., Samal, M. R., & Jose, J. 2018, *ApJ*, 864, 154
- Ebert, R. 1955, *ZAp*, 37, 217
- Evans, N. J. I. 1999, *ARA&A*, 37, 311
- Evans, N. J. I., Dunham, M. M., Jørgensen, J. K., et al. 2009, *ApJS*, 181, 321
- Fang, M., Kim, J. S., van Boekel, R., et al. 2013a, *ApJS*, 207, 5
- Fang, M., van Boekel, R., Bouwman, J., et al. 2013b, *A&A*, 549, A15
- Fang, M., van Boekel, R., King, R. R., et al. 2012, *A&A*, 539, A119
- Flaherty, K. M., Pipher, J. L., Megeath, S. T., et al. 2007, *ApJ*, 663, 1069
- Frerking, M. A., Langer, W. D., & Wilson, R. W. 1982, *ApJ*, 262, 590
- Gaia Collaboration, Brown, A. G. A., Vallenari, A., et al. 2021, *A&A*, 649, A1
- Guo, W., Chen, X., Feng, J., et al. 2021, *ApJ*, 921, 23
- Guo, W., Chen, X., Feng, J., et al. 2022, *ApJ*, 938, 44
- Gutermuth, R. A., Megeath, S. T., Myers, P. C., et al. 2009, *ApJS*, 184, 18
- Hacar, A., Alves, J., Tafalla, M., & Goicoechea, J. R. 2017, *A&A*, 602, L2
- Hacar, A., & Tafalla, M. 2011, *A&A*, 533, A34
- Hacar, A., Tafalla, M., Forbrich, J., et al. 2018, *A&A*, 610, A77
- Hacar, A., Tafalla, M., Kauffmann, J., & Kovács, A. 2013, *A&A*, 554, A55
- Hartmann, L. 2002, *ApJ*, 578, 914
- Henshaw, J. D., Caselli, P., Fontani, F., Jiménez-Serra, I., & Tan, J. C. 2014, *MNRAS*, 440, 2860
- Inutsuka, S.-i., & Miyama, S. M. 1997, *ApJ*, 480, 681
- Jackson, J. M., Finn, S. C., Chambers, E. T., Rathborne, J. M., & Simon, R. 2010, *ApJL*, 719, L185
- Kauffmann, J., Pillai, T., & Goldsmith, P. F. 2013, *ApJ*, 779, 185
- Kauffmann, J., Pillai, T., Shetty, R., Myers, P. C., & Goodman, A. A. 2010, *ApJ*, 716, 433
- Kennicutt, R. C. J. 1998, *ApJ*, 498, 541
- Kirk, H., Myers, P. C., Bourke, T. L., et al. 2013, *ApJ*, 766, 115
- Koenig, X. P., & Leisawitz, D. T. 2014, *ApJ*, 791, 131
- Kroupa, P. 2002, *Sci*, 295, 82
- Krumholz, M. R., & McKee, C. F. 2008, *Natur*, 451, 1082
- Krumholz, M. R., McKee, C. F., & Bland-Hawthorn, J. 2019, *ARA&A*, 57, 227
- Lada, C. J., & Lada, E. A. 2003, *ARA&A*, 41, 57
- Larson, R. B. 1985, *MNRAS*, 214, 379
- Li, S., Sanhueza, P., Lee, C. W., et al. 2022, *ApJ*, 926, 165
- Liu, H.-L., Stutz, A., & Yuan, J.-H. 2019, *MNRAS*, 487, 1259
- Mac Low, M.-M., & Klessen, R. S. 2004, *RvMP*, 76, 125
- Megeath, S. T., Gutermuth, R., Muzerolle, J., et al. 2012, *AJ*, 144, 192
- Megeath, S. T., Gutermuth, R., Muzerolle, J., et al. 2016, *AJ*, 151, 5
- Meyer, M. R., Calvet, N., & Hillenbrand, L. A. 1997, *AJ*, 114, 288
- Milam, S. N., Savage, C., Brewster, M. A., Ziurys, L. M., & Wyckoff, S. 2005, *ApJ*, 634, 1126
- Molinari, S., Swinyard, B., Bally, J., et al. 2010, *A&A*, 518, L100
- Motte, F., Schilke, P., & Lis, D. C. 2003, *ApJ*, 582, 277
- Nagasawa, M. 1987, *PTP*, 77, 635
- Nguyen Luong, Q., Motte, F., Hennemann, M., et al. 2011, *A&A*, 535, A76
- Nguyen-Luong, Q., Nguyen, H. V. V., Motte, F., et al. 2016, *ApJ*, 833, 23
- Ostriker, J. 1964, *ApJ*, 140, 1056
- Palmeirim, P., André, P., Kirk, J., et al. 2013, *A&A*, 550, A38
- Panopoulou, G. V., Clark, S. E., Hacar, A., et al. 2022, *A&A*, 657, L13
- Pecaut, M. J., & Mamajek, E. E. 2013, *ApJS*, 208, 9
- Reid, M. J., & Dame, T. M. 2016, *ApJ*, 832, 159
- Samal, M. R., Ojha, D. K., Jose, J., et al. 2015, *A&A*, 581, A5
- Schneider, N., Csengeri, T., Bontemps, S., et al. 2010, *A&A*, 520, A49
- Schneider, S., & Elmegreen, B. G. 1979, *ApJS*, 41, 87
- Shan, W., Yang, J., Shi, S., et al. 2012, *ITST*, 2, 593
- Shu, F. H., Najita, J. R., Shang, H., & Li, Z. Y. 2000, in *Protostars and Planets IV*, ed. V. Mannings, A. P. Boss, & S. S. Russell (Tucson, AZ: Univ. Arizona Press), 789
- Skrutskie, M. F., Cutri, R. M., Stiening, R., et al. 2006, *AJ*, 131, 1163
- Snell, R. L., Scoville, N. Z., Sanders, D. B., & Erickson, N. R. 1984, *ApJ*, 284, 176
- Solomon, P. M., Rivolo, A. R., Barrett, J., & Yahil, A. 1987, *ApJ*, 319, 730
- Sousbie, T. 2011, *MNRAS*, 414, 350
- Stutzki, J., & Guesten, R. 1990, *ApJ*, 356, 513
- Su, Y., Yang, J., Zhang, S., et al. 2019, *ApJS*, 240, 9
- Sun, Y., Yang, J., Yan, Q.-Z., et al. 2021, *ApJS*, 256, 32
- Treviño-Morales, S. P., Fuente, A., Sánchez-Monge, Á., et al. 2019, *A&A*, 629, A81
- Urquhart, J. S., Moore, T. J. T., Schuller, F., et al. 2013, *MNRAS*, 431, 1752
- Vázquez-Semadeni, E., Palau, A., Ballesteros-Paredes, J., Gómez, G. C., & Zamora-Avilés, M. 2019, *MNRAS*, 490, 3061
- Wang, K., Zhang, Q., Testi, L., et al. 2014, *MNRAS*, 439, 3275
- Wang, S., & Chen, X. 2019, *ApJ*, 877, 116
- Wang, X.-L., Fang, M., Gao, Y., et al. 2022, *ApJ*, 936, 23
- Willis, S., Marengo, M., Allen, L., et al. 2013, *ApJ*, 778, 96
- Wilson, T. L., & Rood, R. 1994, *ARA&A*, 32, 191
- Wouterloot, J. G. A., & Brand, J. 1989, *A&AS*, 80, 149
- Wright, E. L., Eisenhardt, P. R. M., Mainzer, A. K., et al. 2010, *AJ*, 140, 1868
- Wu, J., Evans, N. J. I., Gao, Y., et al. 2005, *ApJL*, 635, L173
- Wu, J., Evans, N. J. I., Shirley, Y. L., & Knez, C. 2010, *ApJS*, 188, 313
- Xiong, F., Chen, X., Yang, J., et al. 2017, *ApJ*, 838, 49
- Xiong, F., Chen, X., Zhang, Q., et al. 2019, *ApJ*, 880, 88
- Yan, Q.-Z., Zhang, B., Xu, Y., et al. 2019, *A&A*, 624, A6
- Yang, J., Fukui, Y., Umemoto, T., Ogawa, H., & Chen, H. 1990, *ApJ*, 362, 538
- Yuan, L., Yang, J., Du, F., et al. 2021, *ApJS*, 257, 51
- Zhang, M., Kainulainen, J., Mattern, M., Fang, M., & Henning, T. 2019, *A&A*, 622, A52
- Zhang, Q., Wang, K., Lu, X., & Jiménez-Serra, I. 2015, *ApJ*, 804, 141